arXiv:0710.4142v1 [astro-ph] 22 Oct 2007

Far-Infrared Spectral Energy Distributions and Photometric Redshifts of Dusty Galaxies

Sukanya Chakrabarti[1,2] & Christopher F. McKee[3]

ABSTRACT

We infer the large-scale source parameters of dusty galaxies from their observed spectral energy distributions (SEDs) using the analytic radiative transfer methodology presented in Chakrabarti & McKee (2005). For local ultra-luminous infrared galaxies (ULIRGs), we show that the millimeter to far-infrared (FIR) SEDs can be well fit using the standard dust opacity index of 2 when self-consistent radiative transfer solutions are employed, indicating that the cold dust in local ULIRGs can be described by a single grain model. We develop a method for determining photometric redshifts of ULIRGs and sub-mm galaxies from the millimeter-FIR SED; the resulting value of $1 + z$ is typically accurate to about 10%. As such, it is comparable to the accuracy of near-IR photometric redshifts and provides a complementary means of deriving redshifts from far-IR data, such as that from the upcoming *Herschel Space Observatory*. Since our analytic radiative transfer solution is developed for homogeneous, spherically symmetric, centrally heated, dusty sources, it is relevant for infrared bright galaxies that are primarily powered by compact sources of luminosity that are embedded in a dusty envelope. We discuss how deviations from spherical symmetry may affect the applicability of our solution, and we contrast our self-consistent analytic solution with standard approximations to demonstrate the main differences.

Subject headings: galaxies: formation—galaxies: starburst—infrared: galaxies—radiative transfer—stars: formation

1. Introduction

The far-infrared (FIR) spectral energy distribution (SED) is a vital implement in understanding the physical conditions of dusty sources. Chakrabarti & McKee (2005, henceforth CM05), presented self-consistent analytic radiative transfer solutions for the spectra of unresolved, homogeneous,

[1]Harvard-Smithsonian Center for Astrophysics, 60 Garden Street, Cambridge, MA 02138 USA; schakrabarti@cfa.harvard.edu

[2]National Science Foundation Postdoctoral Fellow

[3] Departments of Physics and Astronomy, University of California at Berkeley, Mail Code 3411, Berkeley, CA 94720 USA; cmckee@astro.berkeley.edu.

spherically symmetric, centrally heated, dusty sources. We showed that from two colors in the millimeter (mm) and FIR portion of the spectrum one can approximately infer the mm to FIR, and that this in turn determines the luminosity to mass ratio, L/M, and surface density, Σ, which (at low redshift) are distance-independent parameters. With a distance measurement, one can further infer the size, mass, and luminosity of the source. We extensively compared our analytic solutions against a well-tested numerical scheme, DUSTY (Ivezic & Elitzur 1997), to find excellent agreement with the numerical results. Here, we apply this methodology to dusty galaxies to derive their large-scale source parameters. We discuss applications to protostars and radiative transfer methodology of clumpy envelopes in a separate forthcoming paper.

From observations of their SEDs, the IRAS all-sky survey characterized ULIRGs as a class of extremely luminous ($L_{8-1000\ \mu\mathrm{m}} > 10^{12} L_\odot$) galaxies that emit most of their energy in the FIR (Soifer et al. 1984; Aaronson & Olszewski 1984; Soifer et al. 1987; Sanders & Mirabel 1996). These galaxies were then understood to be a new class of objects, quite distinct from those studied by optical surveys as little correlation was found between their optical and infrared luminosities (Sanders & Mirabel 1996). That the demographics of these galaxies is not simply an extrapolation of normal galaxies can be seen from the fact that the luminosity function on the bright end ($L_{\mathrm{IR}} \gtrsim 1 \times 10^{11} L_\odot$) is significantly in excess of the Schechter function (Rieke & Lebofsky 1986). Theoretical models have suggested that heavily starbursting systems like ULIRGs can be produced via mergers of roughly equal mass galaxies (Toomre & Toomre 1972; Mihos & Hernquist 1996), and recent observations corroborate the idea that local ULIRGs are products of major mergers (Dasyra et al. 2006). While the limited sensitivity of IRAS did not allow for a characterization of the redshift evolution of this dusty, luminous population of galaxies, observations by the *Spitzer Space Telescope* indicate that there is a strong evolution in this population (on the basis of near and mid-IR observations converted to total IR luminosities using observational templates) out to $z \sim 1$ (e.g. Le Floch et al. 2005), with the contribution from ULIRGs to the comoving IR energy density increasing by an order of magnitude from local systems to $z \sim 1$.

Understanding the FIR SEDs of dusty galaxies has renewed importance today. Submillimeter galaxies (SMGs; $F_{850\ \mu\mathrm{m}} \gtrsim 1$ mJy) (Ivison et al. 2000; Blain et al. 1998) are luminous ($L \gtrsim 10^{12} L_\odot$), dusty galaxies at moderate redshifts (the median redshift in the Chapman et al. 2003, 2005 samples is $z \sim 2$). They are faint at optical wavelengths and were discovered in the first deep extragalactic surveys in the sub-mm wavebands (the SCUBA Cluster Lens Survey; Smail et al 1997, 2002). SMGs produce a significant fraction of the energy output of the high redshift early universe, and hence represent a cosmologically significant population (Smail et al 1997, Blain et al 2002, Blain et al 1999). Chapman et al. (2005) find that SMGs and Lyman break galaxies contribute equally to the star formation density at $z \sim 2-3$ and that, when extrapolated to lower fluxes, SMGs may be the dominant site of massive star formation at this epoch. Upcoming instruments, such as the *Herschel Space Observatory* and SCUBA-2, will be able to perform routine observations of SMGs at rest-frame FIR wavelengths, which is critical for observationally determining the bolometric luminosities of this high redshift, cosmologically significant population. In contrast to local ULIRGs,

the suggested formation mechanisms and evolutionary scenarios for SMGs remain varied in nature, ranging from primeval, heavily accreting galaxies undergoing a starburst (Rowan-Robinson 2000; Efstathiou & Rowan-Robinson 2003) to products of gas-rich major mergers undergoing intense feedback (Chakrabarti et al. 2007b), with recent observations favoring the latter scenario (Nesvadba et al. 2007; Bouche et al. 2007). In particular, Bouche et al. (2007) suggest that dissipative major mergers may have produced the SMG population on the basis of their finding that the SMG population has lower angular momenta and higher matter densities compared to the UV/optically selected population.

A self-consistent analytic method of inferring source parameters from the observed SEDs may be an useful alternative to SED templates in analyzing upcoming FIR data sets. We give the general relations for observed quantities in terms of the redshift, and graphically depict the variation of these quantities with redshift, which is significant even at $z \sim 1$. We show that this implies that one can estimate the value of $1 + z$ for ULIRGs and SMGs from the mm and FIR SED with an accuracy $\sim 10\%$ (this is comparable to typical accuracies of photometric redshift codes, which estimate z to typical accuracies of $\sim 10\%$, e.g. the IMPZ code of Babbedge et al. 2004, or the widely used HYPERZ code of Bolzonella et al. 2000), given that our assumptions are satisfied: (1) the mm-FIR spectrum is due to reprocessing of emission from a central, dust-enshrouded source; (2) the dust can be approximated as being homogeneous and spherically distributed, with a density that varies as a power of the radius; (3) the source is sufficiently opaque that emission from the dust destruction front is negligible; and (4) the luminosity-to-mass ratio, L/M, of high-redshift ULIRGs and SMGs is similar to that of low-redshift ULIRGs (this last assumption is verified for the small set of SMGs for which adequate data currently exist). Chapman et al. (2005) point out that the dust temperatures inferred for SMGs are significantly lower than those of local ULIRGs and conclude that FIR photometric redshifts have an uncertainty $\Delta z \simeq 1$; as we shall see, our method is significantly more accurate. We primarily focus our discussion of SMGs on sources observed recently by Kovacs et al. (2006) using the 350 μm band of SHARC-2, which is currently the most direct observational probe of the rest-frame FIR of high redshift SMGs.

The organization of the paper is as follows: in §2, we review the basics of the analytic radiative transfer methodology presented in CM05 and collect the main expressions in Appendix A; in §2.1, we explain the general procedure of applying our results, and contrast our solution with standard approximations in Appendix B. §3 is devoted to a treatment of ULIRGs, where we infer the large scale parameters of a dozen local ULIRGs by fitting to the FIR SED. In §4 we present SED fits for a sample of SMGs. In §5 we present the principal result of this paper, a method of inferring redshifts from FIR SEDs, and we demonstrate its applicability both with a simulated test case and with data of SMGs. We conclude in §6. In Appendix B we discuss standard approximations, such as the Hildebrand (1983) prescription for the mass in terms of the mm flux, and modified blackbody single temperature models in fitting the SEDs of ULIRGs and protostars (Yun & Carrilli 2002, henceforth YC02). For purposes of illustration, we graphically contrast our solution and the standard approximations against the numerical results from DUSTY over the astrophysical

parameter space.

2. Analytic SEDs of Dusty Sources

In CM05, we formulated an analytic solution for the FIR SEDs of spherically symmetric, homogeneous dusty sources with a central source of radiation. We considered envelopes that emit most of their radiation at wavelengths longer than 30 μm, and are sufficiently opaque that emission from the dust destruction front does not significantly influence the FIR SED. A corollary to this assumption is that the emergent spectrum is also approximately independent of the temperature of the source of radiation. We did not consider the effects of scattering on the SED, since the scattering efficiency is much smaller than the absorption efficiency at mm and FIR wavelengths. Here, we give a summary of the solution presented in CM05 and collect our expressions for the analytic SED in Appendix A.

We consider power law density variations within the envelope, $\rho(r) \propto r^{-k_\rho}$ and adopt the dust opacity, κ_ν, from Weingartner & Draine (2001, hereafter WD01), with a normalization appropriate for water ice mantles (see eq. 3) For a given density variation in the envelope and dust opacity curve, the emergent spectrum depends on three quantities - the mass of the envelope: $M_{\rm dust} = M/Z_{\rm dust}$, the luminosity, and the radius of the envelope: R. The shape of the SED cannot depend on the distance to the source, and can be specified by two distance-independent parameters, the luminosity to mass ratio, L/M, and the surface density, $\Sigma \equiv M/\pi R^2$.

We defined characteristic parameters, $R_{\rm ch}$ and $T_{\rm ch}$ that are analogous to the Rosseland photosphere and photospheric temperature respectively, such that

$$L \equiv 4\pi \tilde{L} R_{\rm ch}^2 \sigma T_{\rm ch}^4 \ , \tag{1}$$

where $\sigma = 5.67 \times 10^{-5}$ erg cm^{-2} s^{-1} K^{-4} is the Stefan-Boltzmann constant. $\tilde{L}$ is a number of order unity that allows for better agreement with the numerical solutions, particularly for extended atmospheres, which have $\tilde{L} \gtrsim 1$, reflecting the effective increase in emitting area.

The characteristic parameters are determined by requiring that the characteristic optical depth at a frequency $\nu_{\rm ch} \equiv kT_{\rm ch}/h$ equal unity:

$$\tau_{\rm ch} = \kappa_{\nu_{\rm ch}} \int_1^{R_c \to \infty} \rho(\tilde{r}) d\tilde{r} = \frac{\kappa_{\nu_{\rm ch}} \rho(R_{\rm ch}) R_{\rm ch}}{k_\rho - 1} = 1 \ , \tag{2}$$

where $\kappa_{\nu_{\rm ch}}$ is the opacity per unit mass at $\nu_{\rm ch}$ and $\tilde{r} \equiv r/R_{\rm ch}$. Note that this characteristic optical depth is for an effectively infinite shell; it does not take into account the edge of the core at R_c. We assume that $\nu_{\rm ch}$ is within the frequency range where the opacity is approximately a power law:

$$\kappa_\nu = \kappa_{\nu_0} (\nu/\nu_0)^\beta \qquad (30\ \mu{\rm m} \lesssim \lambda \lesssim 1\ {\rm mm}). \tag{3}$$

For $\nu_0 = 3$ THz, corresponding to $\lambda_0 = 100\ \mu$m, we adopt an opacity per unit mass of gas of

$$\kappa_{100\,\mu{\rm m}} = 0.54\delta \quad {\rm cm}^2\ {\rm g}^{-1}. \tag{4}$$

For $\delta = 1$, this is twice the value given by WD01 model for dust in the diffuse interstellar medium since we assume that grains in star-forming regions have ice mantles that double the FIR opacity. The WD01 opacity is based on a gas-to-dust mass ratio of $M/M_d = 105.1$; since the ice mantles most likely have a different opacity per unit mass than the WD01 grains, we do not attempt to infer the dust mass in the sources. Deviations from solar metallicity, or from the assumed dust model, can be taken into account by choosing a different value for δ.

Solving equations (1) and (2) gives the relations between the source parameters, L/M and Σ, and the SED variables, $\tilde{R}_c$ and $T_{\rm ch}$ that govern the shape of the SED:

$$\tilde{R}_c \equiv \frac{R_{\rm c}}{R_{\rm ch}} = \left\{ \frac{(L/M)\Sigma^{(4+\beta)/\beta}}{4\sigma\tilde{L}} \left[\frac{(3-k_\rho)\kappa_{\nu_0}}{4(k_\rho-1)T_0^\beta} \right]^{4/\beta} \right\}^{-\frac{\beta}{2\beta+4(k_\rho-1)}} , \tag{5}$$

and

$$T_{\rm ch} = \left\{ \frac{L/M}{4\sigma\tilde{L}\Sigma^{\frac{3-k_\rho}{k_\rho-1}}} \left[\frac{4(k_\rho-1)T_0^\beta}{(3-k_\rho)\kappa_{\nu_0}} \right]^{\frac{2}{k_\rho-1}} \right\}^{\frac{k_\rho-1}{2\beta+4(k_\rho-1)}} , \tag{6}$$

where $kT_0 \equiv h\nu_0$. We find that

$$\tilde{L} = 1.6\tilde{R}_c^{0.1} \tag{7}$$

is accurate to within ~ 10 % for $1 \lesssim k_\rho \lesssim 2$; note that this value is about twice the value given in CM05. Equations (5) and (6) allow us to *analytically* solve for the distance-independent source parameters once the SED variables are determined from two colors (i.e., flux ratios). We depict in Figure 1 the L/M vs Σ plane overlaid with lines of constant $\tilde{R}_c$ and $T_{\rm ch}$ for the density profile, $k_\rho = 3/2$ and adopted dust model, WD01 coated with ice mantles.

We model the emergent spectrum by assuming that the emission in each frequency channel comes from a shell of thickness $\Delta r_m(\nu)$ centered at a radius $r_m(\nu)$, with a source function $(2h\nu_{ch}^3/c^2)\exp\left[-h\nu/kT(\tilde{r}_m)\right]$ located at an optical depth $\tau_\nu(\tilde{r}_m)$:

$$L_\nu = 4\pi R_{\rm ch}^2 4\pi \left(\frac{2h\nu_{ch}^3}{c^2}\right) \tilde{\kappa}_\nu \tilde{\nu}^3 (k_\rho-1)\tilde{r}_m^{2-k_\rho}\Delta\tilde{r}_m \exp\left[-\frac{h\nu}{kT(\tilde{r}_m)} - \tau_\nu(\tilde{r}_m)\right] , \tag{8}$$

where the optical depth τ_ν from r to the surface of the cloud is

$$\tau_\nu = \tilde{\kappa}_\nu \left(\tilde{r}^{-k_\rho+1} - \tilde{R}_c^{-k_\rho+1}\right) . \tag{9}$$

The FIR emission can be represented with good accuracy with the adoption of a power law for the temperature profile,

$$T = T_{\rm ch}\tilde{r}^{-k_T} . \tag{10}$$

The slope of the temperature profile is determined by imposing the self-consistency condition that the input luminosity exactly equal the emergent luminosity. As expected, the slope of this effective

temperature profile is independent of the optical depth in the limit of low optical depths, and becomes progressively a steeper function of the optical depth for very opaque envelopes. For envelopes that emit most of their flux at wavelengths longer than 30μm, we showed that k_T is a function of $\tilde{R}_c$ only. The functional forms of $k_T(\tilde{R}_c)$ and $\tilde{r}_m$ are given in Appendix A.

We found that spectra are characterized by three frequency regimes, which we denoted as low, intermediate and high. Low and intermediate frequencies are optically thin. Low frequencies are in the Rayleigh-Jeans portion of the spectrum [$h\nu \ll kT(\tilde{R}_c)$] throughout the envelope. The low-frequency emission comes predominantly from the outer parts of the shell and is proportional to the mass. Intermediate frequencies are in the Wien part of the spectrum in the outer envelope, but not near the photosphere. In the intermediate frequency regime, higher frequencies originate from deeper in the envelope, where it is hotter. High frequency photons emanate from a location in the shell that is due to a tug-of-war between the temperature gradient, which favors emission from small radii, and the intervening optical depth, which favors emission from large radii. The forms of the characteristic emission radius, $\tilde{r}_m$ (termed the "contribution function" in CM05) and the thickness, $\Delta\tilde{r}_m$, are given in Appendix A. We illustrate these frequency regimes in Figure 2a with the example of a high-mass protostar from Paper I ($L/M \sim 400 L_\odot/M_\odot$ and $\Sigma \sim 1$ g cm^{-2}); both the analytic and numerical versions of the SED are shown. Figure 2b shows the characteristic emission radius (contribution function) as a function of frequency, and Figure 2c is a plot of the opacity curve, WD01's $R_V = 5.5$ (this curve does not include the effect of ice mantles). One should read these three plots left to right, i.e., follow the marked regions in the SED plot in Figure 2a and correlate them with the marked regions in the contribution function in Figure 2b. The spectral features in the contribution function in Figure 2b correlate with the spectral features in the opacity curve as depicted in Figure 2c. For example, the 10 μm (3×10^{13} Hz) increase in the opacity translates to a corresponding increase in $\tilde{r}_m$, as the $\tau = 1$ surface at this frequency is driven outwards, while the 5 μm (6×10^{13} Hz) decrease in the opacity causes $\tilde{r}_m$ to move inwards.

2.1. Inference of Source Parameters

We solve equations (5) and (6), inserting the relation for $\tilde{L}$ from equation (7), to give the source parameters in terms of SED variables, $T_{\rm ch}$ and $\tilde{R}_c$:

$$\frac{L}{M} = 1.6 \left(\frac{3-k_\rho}{k_\rho - 1}\right) \kappa_{\nu_0} \left(\frac{\sigma T_{\rm ch}^{4+\beta}}{T_0^\beta}\right) \tilde{R}_c^{k_\rho - 2.9} \ , \tag{11}$$

$$\Sigma = \frac{4(k_\rho - 1)}{(3-k_\rho)} \frac{1}{\kappa_{\nu_0}} \left(\frac{T_0}{T_{\rm ch}}\right)^\beta \tilde{R}_c^{\ -(k_\rho - 1)} \ . \tag{12}$$

Since κ_{ν_0} is proportional to the dust-to-gas parameter δ, it follows that we actually infer values for $L/(M\delta)$ and $\Sigma\delta$ from the SED—i.e., the SED is determined by the mass of dust, not gas, in the source. We shall refer to these scaling relations throughout the course of the paper. Our method

for inferring the source parameters depends on whether the redshift is known or not. In either case, we require at least three photometric data points, with at least one in or near each of the three frequency regimes. For example, if there are no data at low frequencies or in the transition region between low and intermediate frequencies, then we can determine only a lower limit on $\tilde{R}_c$; if there are no data at high frequencies or in the transition region between intermediate and high frequencies, then we can determine only a lower limit on $T_{\rm ch}$. If additional data are available we infer the best-fit value for the density profile, k_ρ, as well. We generally find $k_\rho = 2$ for ULIRGs as we show in §3, so we adopt this value if additional data are not available.

First consider sources with known spectroscopic redshifts. For such sources, we transfer the observed data to the rest frame:

$$\nu_{\rm rest} = \nu_{\rm obs}(1+z), \qquad L_{\nu,{\rm rest}} = \frac{4\pi D_L^2 F_{\nu,{\rm obs}}}{1+z} \ . \tag{13}$$

Using the rest-frame values of L_ν, we solve for $\tilde{R}_c$ and $T_{\rm ch}$ and determine the shape of the SED; this allows us to determine the total luminosity, L. Equations (11) and (12) allow us to infer L/M and Σ, which in turn give us M, $R_c = (M/\pi\Sigma)^{1/2}$, and $R_{\rm ch} = R_c/\tilde{R}_c$.

For sources with unknown redshifts, one can fit to the observed-frame fluxes and solve for $\tilde{R}_c$ and $T_{\rm ch}$, and then obtain $(L/M)_{\rm obs}$ and $\Sigma_{\rm obs}$ via equations (11) and (12). As we shall see in §4 below, the observed-frame values of L/M and Σ are quite different from the intrinsic, rest-frame values, and it is possible to estimate the redshift from $(L/M)_{\rm obs}$. With an approximate redshift, one can then infer approximate values for the source parameters, as described above.

We can also approximately obtain the angular size of the photosphere of the sources, even if the redshifts are unknown. The angular size of the photosphere is about $\theta_{\rm ch} \equiv R_{\rm ch}/D_A$, where D_A is the angular diameter distance. We use equation (1) and the relation between the angular diameter distance and the luminosity distance: $D_L = (1+z)^2 D_A$, to write the angular size in terms of the total flux, $F \equiv L/4\pi D_{\rm L}^2$:

$$\theta_{\rm ch} = (1+z)^2 \left(\frac{F}{\tilde{L}\sigma T_{\rm ch}^4}\right)^{1/2} = \left(\frac{F}{\tilde{L}\sigma T_{\rm ch,obs}^4}\right)^{1/2} \ . \tag{14}$$

Thus, we can infer the angular size of the source even if it is unresolved, i.e., we predict the size of the source from observed quantities without knowing the redshift (except for the very weak dependence on $\tilde{L}$).

Many of the sources we consider in this paper may have high-frequency fluxes ($\lambda \lesssim 30$ μm) fluxes that are affected by an inhomogeneous dust envelope, multiple sources of luminosity, and/or an accretion disk. All of these considerations lie outside the scope of the methodology developed in CM05, and to avoid them we perform fits to the mm - 30 μm data, which are unlikely to have been affected. If the resulting model for the SED fits the high-frequency fluxes as well, then that is a good indication that the high frequency emission from the source can also be well-described by our simple theoretical construct.

If the envelope is optically thick at FIR wavelengths and the slope of the temperature profile, k_T, is a strong function of $\tilde{R}_c$, one cannot analytically isolate the unknowns $\tilde{R}_c$ and $T_{\rm ch}$ to express the observed color ratios in terms of the SED parameters. In this case, we have a set of coupled algebraic equations that must be numerically solved, including the uncertainties on the data points, using a least-squares routine. As discussed in CM05, the accuracy for our analytic SED over the astrophysical parameter space, for 1 mm $> \lambda \gtrsim 30$ μm, is generally $\lesssim 30\%$. Our accuracy in the FIR ($300-60$ μm) is typically $\sim 10\%$. If the reported errors on the data points are less than 30% at millimeter wavelengths and less than 10% elsewhere in the spectrum, we artificially increase them to these values in order to account for the intrinsic error in the analytic solution. We report the reduced chi-squared values for both the reported errors and the rescaled errors, if these two values differ dramatically. Rescaling the observed errors to account for the intrinsic error in the analytic solution is analogous to taking an upper bound on the uncertainty. Since the errors in the analytic SED are correlated, the effective uncertainty due to the intrinsic error in the analytic solution and the reported errors for the observed data is less than or equal to the standard deviation of the errors.

As noted in CM05, there are two features of our solution that have not been previously emphasized in the literature. We describe them here in terms of rest-frame quantities. Firstly, extended envelopes (large $\tilde{R}_c$) have a three-component spectrum such that the intermediate frequency component separates cleanly from the low frequency component. The frequency at which this break occurs is termed the break frequency. For large $\tilde{R}_c$, it is given by (see eq. 21 in CM05; note that there is a typographical error, and that the sign of the exponent of $\tilde{R}_c$ should be negative),

$$\tilde{\nu}_{\rm break} = [2.5(2.6-k_\rho)\Gamma\zeta]^{\frac{0.4}{2.6-k_\rho}}\,\tilde{R}_c^{-0.4}\ , \tag{15}$$

where the argument of the Gamma and Zeta functions, $(3-k_\rho)/k_T$, has been suppressed for clarity, and where we have set $k_T = 0.4$, which is appropriate for large $\tilde{R}_c$. We shall find below that the density profile typically corresponds to $k_\rho = 2$; in that case, $\tilde{\nu}_{\rm break} = 1.93\tilde{R}_c^{-0.4}$. The break frequency is comparable to the frequency that corresponds to the temperature at the outer edge of the source, $\nu_c \equiv kT_c/h$, since $\tilde{\nu}_c = T_c/T_{\rm ch} = \tilde{R}_c^{-k_T}$; for the typical case, it is $\nu_{\rm break} = 1.93\nu_c$. The frequency dependence in the intermediate frequency regime ($\nu_{\rm break} < \nu \lesssim \nu_{\rm ch}$) for large $\tilde{R}_c$ is given by:

$$L_\nu \propto \nu^{3+\beta-2.5(3-k_\rho)}\ . \tag{16}$$

Secondly, we presented the ratio of the peak frequency of the SED (expressed as F_ν) in terms of the characteristic frequency. For compact envelopes (low $\tilde{R}_c$), our results are similar to the blackbody limit, with $\nu_{\rm peak} \sim 3\nu_{\rm ch}$, while for extended envelopes, the peak frequency tends to the characteristic frequency. This variation can be approximated by the following form:

$$\frac{\nu_{\rm peak}}{\nu_{\rm ch}} \simeq 0.82k_\rho + \frac{5.4-1.8k_\rho}{\tilde{R}_c^{0.56k_\rho-0.22}}\ , \tag{17}$$

for $1 \lesssim k_\rho \lesssim 2$ to within ~ 20 % accuracy, for $5000 \gtrsim \tilde{R}_c \gtrsim 10$.

3. SEDs & Inferred Parameters for ULIRGs

We present SED fits and source parameters for ten well-known local ULIRGs. Our methodology is most applicable to ULIRGs predominantly powered by a source of luminosity that can be approximated as being compact and nearly enshrouded by dust. Soifer et al. (1999; 2000) found that a large fraction of the mid-infrared emission in a sample of the closest ULIRGs stems from very compact (few hundred parsec) systems, rather than from extended (kiloparsec), weakly obscured starbursts.

High-resolution imaging has revealed many of the complex geometries of merging galaxies (Soifer et al 2000, Goldader et al 2002, Downes & Solomon 1998, Bushouse et al 2002, Scoville et al 1998, Soifer et al 1999, Scoville et al 2000, Surace et al 2000, Surace & Sanders 1999) - in our simple treatment here, we cannot consider these intricate features. Our goal here is to understand the large-scale characteristics of these systems from their FIR SEDs, by approximating them as spherical dust envelopes surrounding a compact central source of luminosity. Recent numerical work by Siebenmorgen & Krugel (2007) on modeling the SEDs of ULIRGs suggests that deviations from spherical symmetry may not significantly affect the FIR SEDs of these systems. Chakrabarti et. al (2007a) solved for the SEDs of ULIRGs using a self-consistent three-dimensional radiative transfer code that takes the gas and stellar densities as input from smoothed particle hydrodynamics simulations, and found that large-scale trends in the FIR SEDs of ULIRGs can by described in terms of these two basic parameters, L/M and Σ, as discussed originally by CM05.

The dust-to-gas ratios in ULIRGs are not entirely certain. The work by Dunne & Eales (2001) found that using two-temperature fits to SEDs leads to dust-to-gas ratios that are closer to Milky Way values than previous work, based on single-temperature fits, had found. Farrah et al. (2005) find (slightly) super-solar metallicities from Space Telescope Imaging Spectrograph (STIS) observations of star-forming knots of dense gas in the nuclear regions of ULIRGs. There are no definitive claims of metallicity gradients in ULIRGs, though one may expect the nuclear regions to be enriched relative to the outer regions; for example, Sodroski et al. (1997) found that the gradient of the dust-to-gas mass ratio is comparable to the metallicity gradient in the Milky Way. Such gradients are also likely to exist in ULIRGs. We quote our results using the local interstellar dust-to-gas ratio (1/105.1, corresponding to $\delta = 1$), but tabulate $M\delta$ so that the results can be readily scaled to different dust-to-gas ratios.

As noted previously, we have used the WD01 dust model, which has a long wavelength dust opacity slope, $\beta = 2$, in performing the fits. Our results show that this fits the long-wavelength points reasonably well (see Figures 3-5). On the other hand, using single-temperature modified blackbody models (e.g. YC02) generally requires $\beta < 2$ to fit the long-wavelength slopes of ULIRGs. Our results for a continuous temperature distribution are consistent with those of Dunne & Eales (2001), who showed that two-temperature blackbodies are enough to fit the spectra with $\beta = 2$. Note that the observed spectrum does not have a slope of 2 in the intermediate frequency regime ($\nu_{\rm break} \lesssim \nu \lesssim \nu_{\rm pk}$; see eqs. 17 and 15).

We discuss some of the ULIRGs in Table 1, beginning with Arp 220, which at a distance of 77 Mpc is the nearest ULIRG and has received the most scrutiny. The nuclear region of Arp 220 has been resolved into a double nucleus (Graham et al 1990) with associated gaseous disks (Downes & Solomon 1998; henceforth DS98) and interpreted to be the result of a merger. The FIR SED of Arp 220 has $F_{100\mu\mathrm{m}} \sim F_{60\mu\mathrm{m}}$, $T_{\mathrm{ch}} \sim 125$ K, and is broad, with $\tilde{R}_c \sim 370$, $R_{\mathrm{ch}} = 30$ pc for $k_\rho = 2$. These SED variables give $\Sigma \sim 0.03$ g cm^{-2}. We estimate a size $R_c \simeq 11$ kpc and $R_{\mathrm{ch}} = 30$ pc for a density profile, $k_\rho = 2$, at a confidence level of 86 %. The large outer radius is needed to fit the mm data. If we allow the density profile parameter to vary, we find that it is constrained to a narrow range of values, $1.7 \lesssim k_\rho \lesssim 2.1$, with the chi-squared per degree of freedom increased by at least one outside these bounds.

From analysis of images of Arp 220 at wavelengths between $3 - 25$ μm, Soifer et al. (1999) noted that fluctuations in seeing could increase the apparent size of the source at these wavelengths, and concluded that the reported FWHM at 24 μm of $0.73''$ (270 pc) (the largest measured diameter among the various wavelengths) could in fact be as small as $0.25''$ (90 pc). We use the analytic methodology of CM05 to compute the characteristic emission radius at 24 μm to find that most of the 24 μm flux is coming from $r \lesssim r_m(24\ \mu\mathrm{m}) = 185$ pc, which is about seven times the characteristic radius. This should be understood as an approximate estimate of the characteristic emission radius at this wavelength, as a clumpy geometry may begin to influence the emergent spectrum somewhat for $\lambda \lesssim 30$ μm; nonetheless, it is consistent with the observations. Early studies of the CO and millimeter dust continuum emission in Arp 220 (e.g. Scoville et al 1991) noted the existence of an extended component, with a size of $7'' \times 15''$ (2.6 kpc $\times$ 5.6 kpc), which is in rough agreement with the overall source size we have derived from the SED.

Dunne & Eales (2001) fit the FIR SED of Arp 220 with a two-temperature blackbody and $\beta = 2$, noting that the masses they infer with the two-temperature fits are a factor of ~ 2 larger than those inferred with single-temperature fits. Our estimate of the outer core temperature, $T_{\mathrm{c}} = 13$ K, is close to their cold-dust temperature of 18 K for Arp 220. In contrast, YC02 fit the FIR SED of Arp 220 with a single-temperature modified blackbody, finding a best-fit $\beta = 1.1$. Our estimate of the mass (4×10^{10} $M_\odot$) is in close agreement with the estimate by Dunne & Eales (2001). Appendix B gives a general explanation for the larger gas masses obtained by Dunne & Eales (2001) and ourselves when using two temperatures or a continuous range of temperatures in fitting the SEDs of extended (large $\tilde{R}_c$) envelopes, in contrast to using a single-temperature blackbody model. DS98 estimated gas masses using a model of subthermally excited CO to fit CO interferometric observations, and derived dynamical masses from their measured line widths and measured CO radii from maps of the CO emission in local ULIRGs. DS98's measurements provide an independent confirmation that the gas density profile varies as r^{-2}. They estimate a gas mass interior to 1.36 kpc of 5.2×10^9 $M_\odot$, while we estimate a gas mass of $4 \times 10^{10}\delta^{-1}$ $M_\odot$ over a radius of 10.3 kpc. Since $M \propto r$ for $\rho \propto r^{-2}$, we infer a gas mass $M(< 1.36\ \mathrm{kpc}) = 5.3 \times 10^9 \delta^{-1} M_\odot$, which is in excellent agreement with their result for $\delta = 1$. These estimates of the gas mass are less than the cited dynamical mass, which in the inner kiloparsec region is dominated by the stars.

It is clear however, that we have significantly underestimated the flux for $\lambda \lesssim 30\ \mu$m . The mid-IR emission is strongly temperature and opacity dependent and would be significantly influenced by the clumpiness of the dust envelope, effects of geometry (the presence of a disk-like structure), and contributions from distributed sources of luminosity, none of which we have accounted for. The contribution from weakly obscured starbursts appears to be ruled out from previous studies (e.g., Soifer et al. 1999; Soifer et al. 2000). We consider the effects of inhomogeneities of the dust envelope and their effects on the high-frequency part of the spectrum in a subsequent paper.

UGC 5101, at a redshift of $z = 0.04$, is thought to contain a buried AGN, based on X-ray observations (Imanishi et al 2003), analysis of PAH and ice-absorption features (Imanishi & Maloney 2003, Imanishi et al 2003), and due to the apparent compactness seen in high resolution imaging (Scoville et al 2000, Soifer et al 2000). *Spitzer* IRS observations of fine structure lines, in particular the high-ionization potential line NeV (the production of which requires energies greater than can be produced by OB stars) further confirm the presence of a buried AGN in this source (Armus et al 2004). UGC 5101 belongs to the new class of XBONGs (X-ray Bright Optically Normal Galaxies) discovered by recent X-ray observations (Maiolino et al 2003, Comastri et al 2002); these surveys uncovered a group of optically elusive AGN that do not show a Seyfert-like spectrum in the optical, but do have a hard X-ray source ($L_{2-10\,\mathrm{keV}} > 10^{41}$erg s^{-1}).

We find a photospheric temperature for this source of $T_{\mathrm{ch}} \sim 110$ K and an outer core temperature of $T_c = 14$ K for a density profile of $k_\rho = 2$ at a confidence level of 43 %. If we allow the density profile to vary, we find that k_ρ is well constrained, with values outside $1.5 \lesssim k_\rho \lesssim 2.1$ being statistically ruled out. We infer a luminosity of $7 \times 10^{11} L_\odot$, a size $R_c \simeq 5$ kpc, and a characteristic radius $R_{\mathrm{ch}} \simeq 34$ pc. As always, our estimate of the total size includes any extended, optically thin emission. Soifer et al. (2000) found that at mid-infrared ($7.9 - 24.5\ \mu$m) wavelengths, the diameter of this source is less than $0.25''$ (205 pc). This is in good agreement with our estimate of the characteristic emission radius at 24 μm, $r_m(24\ \mu\mathrm{m}) \simeq 220$ pc. This is larger than the characteristic radius (34 pc) since the opacity at 24 μm is significantly larger than it is at the characteristic frequency, which corresponds to $\lambda \sim 100\ \mu$m). From our inferred SED parameters, we find that this source has $\Sigma\delta \simeq 0.07$g cm^{-2} and $L/M\delta \simeq 26\ L_\odot/M_\odot$. In contrast to Arp 220, UGC 5101 has $F_{100\mu\mathrm{m}} \gtrsim F_{60\mu\mathrm{m}}$. We infer that it has a lower value of $\tilde{R}_c$ (~ 160 vs. 370) and a higher mean surface density ($\Sigma \sim 0.07$ g cm^{-2} vs. 0.025 g cm^{-2}).

IRAS 08572+3915 differs from the previous two sources in having $F_{100\mu\mathrm{m}} < F_{60\mu\mathrm{m}}$. This source appears to contain an AGN based on an analysis of PAH features (Imanishi & Dudley 2000) and on the compactness seen from imaging (Surace et al 1998, Soifer et al 2000). It is the warmest ($T_{\mathrm{ch}} \sim 170$K) source in our sample, with $L/M\delta = 128\ L_\odot/M_\odot$, and the lowest value of the surface density, $\Sigma\delta \sim 0.01$ g cm^{-2}. As previously, we have solved for these parameters simultaneously, along with the density variation, which yields a best-fit density profile of $k_\rho = 2$ at a confidence level of 83 %. Density profiles greater than 2.1 and less than 1.7 are not favored statistically.

Density profiles of $k_\rho = 2$ are supported by the resolved observations of DS98 for other sources

in our sample as well. Furthermore, our mass estimates based on dust emission are in good agreement with those of DS98, which are based on CO emission. As noted earlier, our estimate of the mass for Arp 220 is in excellent agreement with that measured by DS98. Resolved observations of Mrk 231 yield a gas mass very similar to ours; they estimate a gas mass interior to 1.7 kpc of $4 \times 10^9 M_\odot$, which is within a factor of 1.5 of our estimate for $r < 1.7$ kpc. DS98 cite a mass for IRAS 10565+2448 of 4×10^9 $M_\odot$ for $r < 1.6$ kpc which is within a factor of 1.5 of our value for the mass enclosed interior to that radius. On average, our estimates of the mass (based on $\delta = 1$) are about 1.3 times those of DS98, which is excellent agreement in view of the uncertainties in each method and of possible variations in the value of δ from galaxy to galaxy.

4. Inferred Parameters for Sub-millimeter Galaxies

We present here our SED fits and inferred parameters for several SMGs. We focus our discussion of the SEDs of SMGs on the observations of Kovacs et al. (2006), which make use of SHARC-2 350 μm measurements; these are currently the most direct probe of the rest-frame FIR for $z \sim 2$ systems. The SEDs of these sources are shown in Figures 8-12 and the source and SED parameters are reported in Table 2. For sources for which there are no data shortwards of the peak, we set bounds on $\tilde{R}_c$ guided by our experience with local ULIRGs, i.e., specifically we set the minimum and maximum values to be 40 and 600, respectively, which encompasses the range of values of $\tilde{R}_c$ that we found for local ULIRGs. We take $k_\rho = 2$ for all of these sources, as we found that $k_\rho = 2$ provided the best fit to the data of local ULIRGs and is independently supported by CO observations of DS98.

Recall that the break frequency, $\nu_{\rm break}$, is the frequency at which the emission changes in character from being dominated by the cool material on the outside to warmer material that is deeper inside the envelope. For the ULIRGs listed in Table 1, the typical break frequency is $\nu_{\rm break} \simeq 1 \times 10^{12}$ Hz. However, note that moving a local ULIRG to higher redshift moves the break frequency to lower frequencies by a factor of $(1+z)$—which means that even mm wavelengths can be in the intermediate frequency region for high-redshift systems such as SMGs. Normalizing to a typical value of $\tilde{R}_c \sim 100$, we find from equation (15) that

$$\nu_{\rm break} = 6.35 \times 10^9 \left(\frac{100}{\tilde{R}_c}\right)^{0.4} \frac{T_{\rm ch}}{1+z} \quad {\rm Hz}, \tag{18}$$

for a typical value of the density profile, $k_\rho = 2$. For frequencies less than this break frequency, the slope of the spectrum transitions to the low frequency (Rayleigh-Jeans) regime and one may use equation (B5) to solve for the mass given the millimeter flux.

For the source SMMJ163658.19+410523.8 from Kovacs et al. (2006) (abbreviated as SMMJ1636581 in Table 2), which is at $z = 2.454$, we estimate a luminosity in the range of $6.8 - 8.2 \times 10^{12} L_\odot$, which is close to the estimate of $8.5 \times 10^{12} L_\odot$ cited by Kovacs et al. (2006), which they obtained by fitting a modified greybody to the observed SED. The range of values for which the chi-squared per degree

of freedom changes by less than unity for $\tilde{R}_c$ and $T_{\rm ch}$ are $40-150$ and $103-115$ K, respectively. The large uncertainties in the determination of the SED quantities and the corresponding source parameters, particularly the surface density are due to this source having a rest-frame SED that peaks at a wavelength shorter than the observed 350 μm band. *Herschel* PACS observations (the 170 μm band) are needed to firmly constrain the SED and source parameters of this galaxy.

We find that the source SMMJ13650.43+405737.5, which is at $z = 2.378$ has a luminosity of $5 \times 10^{12} L_\odot$, also quite close to the value cited by Kovacs et al. (2006). This source peaks at a longer wavelength, and SHARC-2 observations are sufficient to more firmly constrain the SED and source parameters. Finally, the source SMMJ105238, which is the highest redshift SMG among these sources ($z_{\rm spec} = 3.036$), has a rest-frame SED that peaks at the shortest wavelength, and therefore has the highest $T_{\rm ch}$ of any source in this sample. Our inferred size, 13.4 kpc, is also larger than what we found for the other sources.

Due to the small number of rest-frame FIR observations of $z \sim 2$ SMGs, our sample of galaxies studied here is necessarily limited. Nonetheless, there are several trends that do stand out. The SMGs we have studied have higher luminosities than local ULIRGs by a factor of 5.5 on average, i.e., the luminosities are all in excess of $4 \times 10^{12} L_\odot$. The gas masses are also higher than local ULIRGs by a factor of ~ 8, but the geometric mean luminosity-to-mass ratio of these galaxies is $\simeq 40$, which is within a factor 1.4 of that of local ULIRGs (see below); the scatter in L/M about this mean is less than a factor 2.

5. FIR Photometric Redshifts

Chapman et al. (2003, 2005) have been very successful at obtaining spectroscopic redshifts of SMGs from optical measurements, guided by radio or optical associations. This approach has yielded about a hundred accurate spectroscopic redshifts. However, spectroscopic redshifts may not be available for the large samples of SMGs that are expected to be observed by upcoming FIR instruments like *Herschel*. We present here a means of inferring the redshifts of dusty galaxies from FIR photometric data. We present the derivation of this method both using our formalism and using very simple relations that are independent of the details of our formalism.

The parameters we infer, L/M and Σ, depend on redshift through the dependence of frequency on redshift. We can express the redshift dependence of these parameters in a very simple manner. Since the luminosity of a dust envelope satisfies $L \propto R^2 T^4$ and the inferred mass is $M \propto \Sigma R^2$, we have:

$$\frac{L}{M} \propto \frac{T^4}{\Sigma} \ . \tag{19}$$

The redshift dependence of the surface density, Σ, follows from noting that the optical depth at the observed frequency must match that at the emitted frequency, since τ_ν determines the shape of the SED, which is invariant: $\kappa(\nu_{\rm obs})\Sigma_{\rm obs} = \kappa(\nu_{\rm rest})\Sigma_{\rm rest}$, so that $\Sigma_{\rm obs}/\Sigma_{\rm rest} = (\nu_{\rm rest}/\nu_{\rm obs})^\beta = (1+z)^\beta$.

Since $T_{\rm obs} = T_{\rm rest}/(1+z)$, it follows that

$$\left(\frac{L}{M\delta}\right)_{\rm obs} = \left(\frac{L}{M\delta}\right)_{\rm rest} (1+z)^{-(4+\beta)} \ , \tag{20}$$

where we have included the dust-to-gas parameter δ to emphasize that we are actually determining the dust mass.

Alternatively, we can derive the redshift dependence of L/M within the context of our formalism. Using $\nu_{\rm ch,\,obs} = \nu_{\rm ch,\,rest}/(1+z)$ in equations (11) and (12), and noting that $\tilde{R}_c$ is independent of redshift since it is a dimensionless ratio of two lengths, it is straightforward to show that:

$$\Sigma_{\rm obs} = \Sigma_{\rm rest}(1+z)^{\beta}, \qquad \left(\frac{L}{M\delta}\right)_{\rm obs} = \left(\frac{L}{M\delta}\right)_{\rm rest} (1+z)^{-(4+\beta)} \ . \tag{21}$$

Figure 6 shows the change in these parameters, when a local ULIRG ($z \ll 1$), with inferred parameters similar to Arp 220, is moved to $z = 1$. Note that the line along which the source is moving as a function of redshift is a line of constant $\tilde{R}_c$. The parameters reported in Table 1 (and Table 2 for SMGs) are the intrinsic parameters; observed parameters can be obtained by using the relations in equation (21) along with the redshifts cited for the sources.

We can now use equation (21) or (20) to infer the redshift of a dusty galaxy from its observed value of $L/M\delta$, which we have shown can be derived from the FIR SED analytically:

$$1 + z_{\rm inf} = \left[\frac{\langle L/M\delta\rangle}{(L/M\delta)_{\rm obs}}\right]^{1/6} \ , \tag{22}$$

where $\langle L/M\delta\rangle$ is the typical value; since $L/M\delta$ can range over an order of magnitude, we use the geometric mean. Note that L is the FIR luminosity, which is determined by our analytic fit to data at rest wavelengths $\gtrsim 60$ μm. Here we have taken advantage of the result that $\beta \simeq 2$. For $L/M\delta$ within a factor 3 of the mean, the uncertainty in $1+z$ is only $3^{1/6} = 1.20$.

The geometric mean of the intrinsic $L/M\delta$ values of the ULIRGs in Table 1 is $\langle L/M\delta\rangle = 60\ L_\odot/M_\odot$; all the ULIRGs in our sample have $L/M\delta$ within a factor 3 of this. The inferred redshift for a ULIRG at high redshift is then

$$1 + z_{\rm inf} = \left[\frac{60}{(L/M\delta)_{\rm obs}}\right]^{1/6} \qquad \text{(ULIRG normalization)} \tag{23}$$

As we show below, the typical uncertainty for deriving redshifts for SMGs using this normalization is $\sim 10\%$.

To demonstrate the applicability of our redshift inference method, we first infer the redshift for a test case where we know the redshift exactly. We place the observed SED of Arp 220 at a range of redshifts, from $z = 0.018 - 10$ (Fig 7a), and use our method to infer the redshift. To test the sensitivity of our method to redshift, we first replace $\langle L/M\delta\rangle$ with the value for Arp 220 and

infer $(1+z_{\rm inf})/(1+z)$, where $z_{\rm inf}$ refers to our inferred redshift and z is the actual redshift (Fig 7b). We find that $0.95 < (1+z_{\rm inf})/(1+z) < 1$, which demonstrates that in principle our method should work out to redshifts $z \sim 10$. Next, we use our method with the mean value of $L/M\delta$ (eq. 23); since Arp 220 has a relatively low light-to-mass ratio ($L/M\delta \simeq 25$), the inferred redshift is somewhat higher than the actual one, $1.09 < (1+z_{\rm inf})/(1+z) < 1.15$.

We now infer the redshifts for a sample of SMGs at $z \sim 2-3$ studied recently by Kovacs et al. (2006) using SHARC-2 350 μm measurements (which probe close to the rest-frame FIR for $z \sim 2$ galaxies), and SCUBA and MAMBO measurements. We illustrate our method with two different normalizations. Prior to the determination of spectroscopic redshifts for the SMGs, they would most likely have been compared with local ULIRGs; their FIR photometric redshifts could have then been determined from equation (23). Now that redshifts have been measured for some of the SMGs, it is also possible to use a normalization appropriate for them:

$$1+z_{\rm inf} = \left[\frac{40}{(L/M\delta)_{\rm obs}}\right]^{1/6} \qquad \text{(SMG normalization)} \ . \tag{24}$$

Note that once a larger sample of SMGs with measured SEDs and spectroscopic redshifts becomes available, it will be possible to improve the accuracy of the average $L/M\delta$ for SMGs in this equation. We compare our estimated redshifts using both normalizations with the measured spectroscopic redshifts in Table 3. We define the accuracy of the redshift determination as

$$A \equiv \frac{{\rm Max}(1+z, 1+z_{\rm inf})}{{\rm Min}(1+z, 1+z_{\rm inf})} \ . \tag{25}$$

The average accuracy of the redshifts using the ULIRG normalization for the sources in Table 3 is $\langle A \rangle = 1.11$. Using the SMG normalization, the average accuracy improves to 1.05.

An alternate method of inferring redshifts utilizing FIR photometry is to infer the redshift from the longwards shift in the observed-frame peak of the SED (e.g., Chapman et al. 2005). There are two problems with this: First, it is difficult to determine the peak frequency accurately from poorly sampled, noisy data. Second, the intrinsic range of values of $T_{\rm ch}$ is larger than the range of values of $(L/M\delta)^{1/6}$. For the sample of ULIRGs in Table 1, $T_{\rm ch}$ varies by a factor 1.3 from the average value of 132, whereas $(L/M\delta)^{1/6}$ varies only by a factor 1.20. For the sample of SMGs in Tables 2 and 3, $T_{\rm ch}$ varies by a factor 1.22 from the mean, whereas the inferred redshifts from our method are accurate to within a factor 1.15 and 1.08 (at worst; the typical accuracies are 1.1 and 1.05 respectively) using the ULIRG normalization and the SMG normalization, respectively. Thus, in each case the $L/M\delta$ method gives a value of $1+z$ that is more accurate by a factor of about 1.5.

We note that an important caveat to applying our redshift estimation method is that normal galaxies at low redshifts that have lower star formation rates than ULIRGs and have intrinsically lower $L/M\delta$ values can be misidentified as high redshift ULIRGs, if only FIR data are available. This problem can be remedied through the use of multi-wavelength photometry. Dusty ULIRGs radiate most of their energy in the infrared, so intrinsically low $L/M\delta$ galaxies can be identified by

comparing the near-IR (or UV/optical) photometry with the FIR, so as to select only those where the latter dominates.

The Infrared Array Camera (IRAC) on board the *Spitzer Space Telescope* has been instrumental in obtaining photometric redshifts (Brodwin et al. 2006) of high redshift galaxies. This method primarily utilizes the approximate constancy of the rest-frame stellar peak at $\lambda = 1.6$ μm (Simpson & Eisenhard 1999; Sawicki 2002). Although near-IR photometric redshift codes are highly successful and sophisticated, utilizing template fitting Monte Carlo algorithms or neural networks, a key component of these various algorithms is to sample the 1.6 μm stellar peak, which cannot be accomplished for $z \gtrsim 4$ by IRAC. Moreover, these codes generally have difficulty in obtaining robust photometric redshifts for power-law AGN-type near-IR SEDs, where the stellar bump is weak or absent. As such, many photometric redshift codes calibrate their methods on SED samples that exclude AGN-type SEDs. By contrast, several of the sources in our local ULIRG sample are optically classified quasars, such as Mrk 1014 and Mrk 231, while others such as IRAS 08572+3915 are inferred to have energetically active AGN on the basis of hard X-ray measurements. Our FIR photometric redshift method may be useful as a complementary technique for sources with AGN. These sources do have somewhat larger values of $L/M\delta$ (by about a factor of 2 relative to the geometric mean of $L/M\delta$). It is possible that when larger sets of FIR observations of high redshift ULIRGs become available with *Herschel* and SCUBA-2 observations, one may be able to robustly identify two subclasses of sources, corresponding to galaxies with energetically active AGN (~ 2 times higher $L/M\delta$) and those without energetically active AGN. Inferring photometric redshifts within these subclasses with the appropriate $L/M\delta$ may further improve the accuracy.

6. Conclusions

We have applied the shell methodology for radiative transfer developed in CM05 to a range of extragalactic sources, from local ULIRGs to high redshift SMGs. The main results are:

1. Using the general expressions for the SEDs of dusty sources given in CM05, we have shown how to derive the light-to-mass ratio, $L/M\delta$, and the mean surface density, $\Sigma\delta$, of dusty galaxies at cosmological distances. Here M and Σ refer to the gas mass, and L is the FIR luminosity as determined from observations at rest wavelengths $\gtrsim 60$ μm. The effective dust-to-gas ratio, δ, is the ratio of the actual FIR opacity to the one we have adopted, which is twice the Weingartner & Draine (2001) opacity; the factor 2 allows for ice mantles. Approximate expressions are given for the case in which the radius of the dusty envelope, R_c, is much larger than the characteristic photospheric radius, $R_{\rm ch}$ (i.e., for $\tilde{R}_c \equiv R_c/R_{\rm ch} \gg 1$).

2. The long-wavelength slope of ULIRGs can be fit with a standard dust opacity curve ($\kappa_\nu \propto \nu^2$ in the FIR) when a self-consistent radiative transfer solution is employed. This confirms the conclusion of Dunne & Eales (2001), who used two-temperature fits to the SED. Comparison with the three sources in DS98 for which there are resolved measurements for the galaxies in our sample

(Arp 220, Mrk 231 and IRAS 10565+2448) shows that on average our mass estimates are about 1.3 times greater than theirs, which is excellent agreement in view of the approximations in each method and the possible variations in the value of δ from galaxy to galaxy.

3. From an analysis of the FIR data of 10 local ULIRGs, we find that the mm to FIR SED can be well-described by our simple construct of a spherically symmetric dust envelope surrounding a central source of luminosity. We find that a density profile $\rho \propto r^{-2}$ provides the best to the FIR data and is consistent with CO masses. We report our findings for the luminosities, masses, and sizes of these 10 ULIRGs.

4. We find that local ULIRGs and high redshift SMGs ($z \sim 2$) have similar $L/M\delta$ ratios, with the SMGs in our sample having values ~ 1.45 times smaller. The SMGs in our sample have luminosities about 5.5 times larger, and masses about 8 times larger, than the ULIRGs in our sample.

5. We have developed a method of inferring FIR photometric redshifts. The accuracy of the method depends on whether the galaxy has a light-to-mass ratio comparable to the template, but since $1+z$ scales as only the 1/6 power of $L/M\delta$, significant variations are allowed. Using Arp 220 as an example, we showed that our method should work for redshifts $z \lesssim 10$. We tested our method on a sample of five SMGs for which good photometric data are available. Under the assumption that the SMGs had the same light-to-mass ratio as a sample of local ULIRGs, we were able to infer values of $1+z$ for the SMGs with an average accuracy of 10% and a worst accuracy of 15%. If we used the average light-to-mass ratio for the SMGs, the average accuracy improved to about 5%. As the samples of high-redshift galaxies grow, our knowledge of both the typical light-to-mass ratio and the accuracy of FIR photometric redshifts will improve. Our method should be applied to galaxies that radiate most of their energy in the FIR, such as ULIRGs and SMGs. Whether this condition is met can be determined by confirming that the near-IR (or optical/UV) luminosity is significantly less than that emerging in the FIR. Our method works even if AGN provide a significant fraction of the luminosity, although our sample is not large enough to determine how large the AGN fraction can become before our method breaks down. As our method is analytic, it can be employed to quickly obtain photometric redshifts of large samples of SMGs, as are expected to be detected in the FIR by the upcoming *Herschel* mission. This FIR photometric redshift method provides a complementary means of inferring the redshift when near-IR methods are not available or are not viable.

6. We discuss how our approximation for the radiative transfer compares with the standard single-temperature SED in Appendix B. The accuracy of the single-temperature blackbody approximation degrades for extended envelopes, $\tilde{R}_c \gtrsim 100$, but the approximation is typically accurate to within a factor 2 for compact envelopes, for which the source function does not probe a large range of temperatures. The effective dust temperature in the single-temperature approximation is close to the outer core temperature.

We thank Henrik Beuther, Jack Welch, Carl Heiles, Phil Myers, Jonathan Tan, Susana Lizano, Dave Sanders, Yeshe Fenner, and Ski Antonucci for helpful discussions. We especially thank Erik Rosolowsky for many helpful and informative discussions on the inference of gas masses and CO observations. The research of CFM is supported in part by the NSF through grants AST06-06831, and PHY05-51164. The research of SC is supported by a National Science Foundation postdoctoral fellowship.

A. Analytic SEDs

Here we summarize the analytic form for the mm to far-IR SED derived in CM05:

$$L_\nu = 16\pi^2(k_\rho - 1)R_{\rm ch}^2\left(\frac{2h\nu_{ch}^3}{c^2}\right)\tilde{\kappa}_\nu\tilde{\nu}^3\tilde{r}_m^{2-k_\rho}\Delta\tilde{r}_m \exp\left[-\frac{h\nu}{kT(\tilde{r}_m)} - \tau_\nu(\tilde{r}_m)\right] \ . \tag{A1}$$

The optical depth, τ_ν is given by:

$$\tau_\nu = \tilde{\kappa}_\nu\left(\tilde{r}^{-k_\rho+1} - \tilde{R}_c^{-k_\rho+1}\right) \ . \tag{A2}$$

The temperature profile, $T(\tilde{r}_m)$, is given by $T = T_{\rm ch}\tilde{r}^{-k_T}$, with k_T and $\tilde{r}_m$ specified below.

The characteristic normalized emission radius, $\tilde{r}_m(\nu)$, is the location in the shell where most of the flux in a given frequency-band originates from, (the "m" is for maximum), and is given by

$$\tilde{r}_m = {\rm Min}\left(\tilde{r}_{\rm m,low-int} + \tilde{r}_{\rm m,high}, \tilde{R}_c\right) \ , \tag{A3}$$

where the total $\tilde{r}_m$ is the sum of the high frequency $\tilde{r}_m$ and the combined low-intermediate frequency $\tilde{r}_m$,

$$\tilde{r}_{\rm m,high} = \left[\frac{\tilde{\kappa}_\nu(k_\rho - 1)}{\tilde{\nu}k_T}\right]^{1/(k_T+k_\rho-1)} \ , \tag{A4}$$

$$\tilde{r}_{\rm m,low-int} = \frac{\tilde{R}_c C^{1/k_T}}{\tilde{R}_c\tilde{\nu}^{1/k_T} + C^{1/k_T}} \ . \tag{A5}$$

The parameter C is the ratio of the typical value $h\nu$ to kT in the intermediate frequency regime, and is given by

$$C = 0.3 + 1.5k_\rho - 0.78k_\rho^2 \ . \tag{A6}$$

The power law for the temperature profile is approximately

$$k_T = \frac{0.48k_\rho^{0.05}}{\tilde{R}_c^{0.02k_\rho^{1.09}}} + \frac{0.1k_\rho^{5.5}}{\tilde{R}_c^{0.7k_\rho^{1.9}}} \ . \tag{A7}$$

The preceding two relations hold for $1 \lesssim k_\rho \lesssim 2$ and $\tilde{R}_c \gtrsim 2$ to within ~ 10 % accuracy.

The shell thickness, $\Delta\tilde{r}_m$ is given by:

$$\Delta\tilde{r}_m = \left[\frac{\Gamma\zeta\exp\left(\tilde{\nu}\tilde{r}_{m,\,\mathrm{low-int}}^{k_T}\right)}{(3-k_\rho-k_T)\tilde{\nu}\Gamma\zeta\tilde{R}_c^{-(3-k_\rho-k_T)}+k_T\tilde{\nu}^{(3-k_\rho)/k_T}}\right]\frac{1}{\tilde{r}_{m,\,\mathrm{low-int}}^{2-k_\rho}} + \frac{(2\pi/h''_m)^{1/2}}{1+2\tilde{\kappa}_\nu\left(\frac{k_\rho-1}{k_\rho+1}\right)\left(\tilde{r}_{m,\,\mathrm{high}}^{1-k_\rho}-\tilde{r}_{m,\,\mathrm{high}}^{2}\tilde{R}_c^{-k_\rho-1}\right)}\ , \tag{A8}$$

where the argument $(3-k_\rho)/k_T$ for the Gamma and Zeta functions has been suppressed for clarity and where

$$h''_m = \tilde{\nu}k_T(k_T-1)\tilde{r}_{\mathrm{m,high}}^{k_T-2} + k_\rho(k_\rho-1)\tilde{\kappa_\nu}\tilde{r}_{\mathrm{m,high}}^{-k_\rho-1}\ . \tag{A9}$$

B. Inference of Masses from the Low-frequency Dust Continuum

It is possible to infer the mass of gas in a source of known redshift directly from the observed flux and quantities that describe the SED. At low frequencies ($\nu < \nu_{\mathrm{break}}$), the source is both optically thin and the temperature is high enough that the emitted radiation is in the Rayleigh-Jeans regime. As a result, the spectral luminosity is

$$L_\nu = \int_{R_d}^{R_c}(4\pi\rho\kappa_\nu B_\nu)4\pi r^2 dr\ , \tag{B1}$$

where the Planck function $B_\nu = 2kT/\lambda^2$ in the Rayleigh-Jeans regime. Dust sublimates inside the dust destruction radius R_d, and we assume that this is negligible compared to the size of the source, R_c. For power-law density and temperature profiles, $\rho = \rho_{\mathrm{ch}}\tilde{r}^{-k_\rho}$ and $T = T_{\mathrm{ch}}\tilde{r}^{-k_T}$, we then find

$$L_\nu = 4\pi\rho_{\mathrm{ch}}\kappa_\nu\left(\frac{2kT_{\mathrm{ch}}\nu^2}{c^2}\right)4\pi R_{\mathrm{ch}}^3\left(\frac{\tilde{R}_c^{3-k_\rho-k_T}}{3-k_\rho-k_T}\right)\ . \tag{B2}$$

This result also follows directly from equations (4), (12) and (16) in CM05. The mass of gas producing the emission is

$$M = \int_0^{R_c}4\pi r^2\rho_{\mathrm{ch}}\tilde{r}^{-k_\rho}dr = 4\pi\rho_{\mathrm{ch}}R_{\mathrm{ch}}^3\left(\frac{\tilde{R}_c^{3-k_\rho}}{3-k_\rho}\right)\ . \tag{B3}$$

Noting that the temperature at the outer edge is $T_c = T_{\mathrm{ch}}\tilde{R}_c^{-k_T}$, we can relate the mass to the luminosity,

$$M = \left(1-\frac{k_T}{3-k_\rho}\right)\left(\frac{c^2}{8\pi kT_c}\right)\frac{L_\nu}{\nu^2\kappa_\nu}\ . \tag{B4}$$

To this point, all frequencies are measured in the rest frame of the source. Converting to observed frequencies and using equation (13), we can relate the mass to the observed flux,

$$M = \left(1-\frac{k_T}{3-k_\rho}\right)\left(\frac{c^2}{2kT_{c,\,\mathrm{rest}}}\right)\frac{D_L^2F_{\nu\,\mathrm{obs}}}{(1+z)^3\nu_{\mathrm{obs}}^2\kappa[(1+z)\nu_{\mathrm{obs}}]}\ , \qquad ([\nu_{\mathrm{obs}}(1+z)<\nu_{\mathrm{break}}], \tag{B5}$$

where $\nu_{\rm break}$ is given by equation (15) or, for the case $k_\rho = 2$, by equation (18). Note that this expression for the mass depends on only one parameter from the SED, the temperature at the edge of the core, $T_{c,\,\rm rest} = T_{\rm ch,\,rest}\tilde{R}_c^{-k_T}$.

One of the standard approximations used in the literature to infer source parameters from SEDs is Hildebrand's (1983) approximation, where one assumes an isothermal distribution of dust. To illustrate the difference between our solution, which self-consistently takes into account the temperature variation in the envelope, and the standard Hildebrand solution, we over-plot our solution with DUSTY's numerical results for a large $\tilde{R}_c$ case, $\tilde{R}_c \sim 300$, and a small $\tilde{R}_c$ case, $\tilde{R}_c \sim 10$, in Figures 13 and 14. As is clear, the accuracy of such single-temperature fits, relative to the numerical solution, degrades for large $\tilde{R}_c$, but is nearly as accurate as our solution for low $\tilde{R}_c$. Similarly, the inference of source parameters using Hildebrand's prescription also degrades at large $\tilde{R}_c$ to a factor of ~ 2, while our solution is accurate (for this large $\tilde{R}_c$ example) to within 10 %.

If we wanted to characterize the envelope as having a single temperature, we can see from equation (B4) that that equivalent temperature is

$$T_{\rm dust} = \left(1 - \frac{k_T}{3 - k_\rho}\right)^{-1} T_c \ , \tag{B6}$$

where for the remainder of this discussion we shall assume $z = 0$ and where $T_{\rm dust}$ is now the *single* temperature characterizing the entire envelope, and not the photospheric temperature, which has a particular meaning (see CM05). However, this is not the temperature that one uses when one uses the Hildebrand approximation (or single-temperature blackbody approximation). Instead, one uses the frequency at which the spectrum peaks, which for a modified blackbody is $h\nu_{\rm peak} = (3+\beta_{\rm iso})kT$, where $\beta_{\rm iso}$ is the value of the opacity index used in the isothermal fit. For an isothermal dust distribution ($k_T = 0$ and $T = T_{\rm dust}$), we can rewrite equation (B4) in terms of the peak frequency as

$$M_{\rm iso} = \left[\frac{(3+\beta_{\rm iso})c^2}{8\pi h\nu_{\rm peak}}\right]\frac{L_\nu}{\nu^2\kappa_\nu} \ . \tag{B7}$$

The value of $\beta_{\rm iso}$ used in single temperature solutions is often ~ 1 (Yun & Carilli 2002, Dunne & Eales 2000).

To understand why the Hildebrand approximation deviates from our solution (and the numerical solution) at large $\tilde{R}_c$, we express the ratio of our mass estimate to the isothermal estimate as

$$\frac{M}{M_{\rm iso}} = \left(1 - \frac{k_T}{3 - k_\rho}\right)\frac{\tilde{\nu}_{\rm peak}\tilde{R}_c^{k_T}}{(3+\beta_{\rm iso})} \ , \tag{B8}$$

where we used the relation $h\nu_{\rm peak}/kT_c = h\nu_{\rm peak}\tilde{R}_c^{k_T}/kT_{\rm ch} = \tilde{\nu}_{\rm peak}\tilde{R}_c^{k_T}$. In general, the peak frequency is a function of $\tilde{R}_c$, as we have discussed in CM05; for $k_\rho = 2$ and large $\tilde{R}_c$, it approaches 1.64 (eq. 17). For large $\tilde{R}_c$, we have $k_T \simeq 0.4$, which for $\beta_{\rm iso} = 1$ implies that $M/M_{\rm iso} \simeq (\tilde{R}_c/30)^{0.4}$. Hence, the isothermal approximation becomes increasingly inaccurate as $\tilde{R}_c$ increases. This is to be expected, since emission arises from a wide range of radii when the envelope is very distended, with $R_c \gg R_{\rm ch}$.

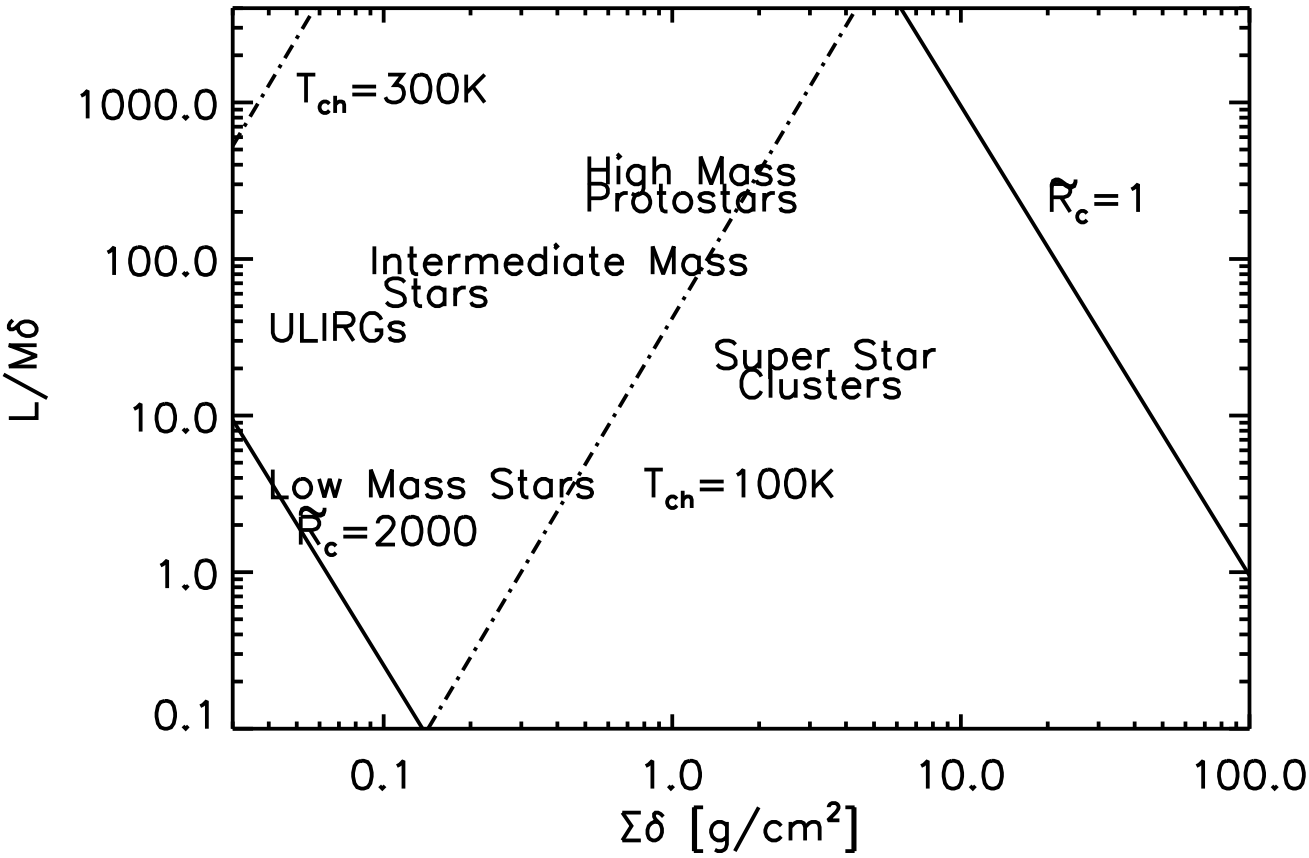

Fig. 1.— $L/M\delta$ vs $\Sigma\delta$ plot for density profile, $k_\rho = 3/2$ and dust model, Weingartner & Draine (2001) coated with ice mantles

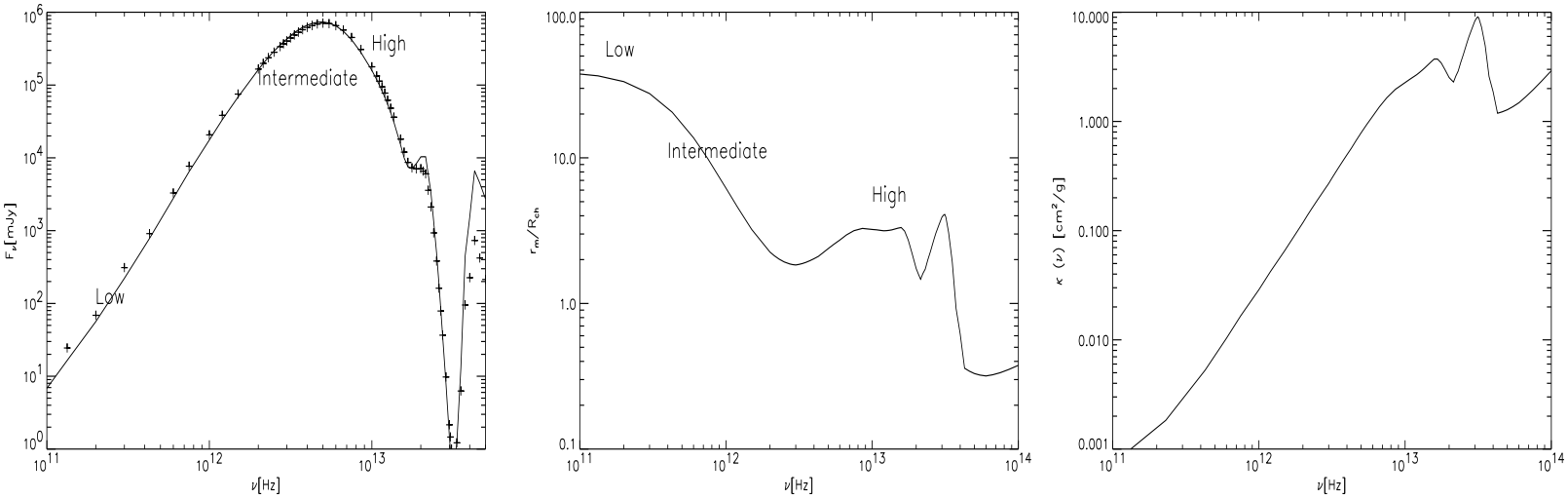

Fig. 2.— (a) SED for typical high-mass protostar with frequency regimes marked (solid line is DUSTY SED and crosses analytic SED). (b) Contribution function (the characteristic emission radius) in dimensionless units, $\tilde{r}_m$, with frequency regimes marked. (c) WD01 opacity curve. The spectral features in the SED and opacity curve as shown in (a) and (c), e.g. the 3×10^{13}Hz (10μm) absorption feature, correlate with the location in the envelope this emission is coming from, as shown in (b)

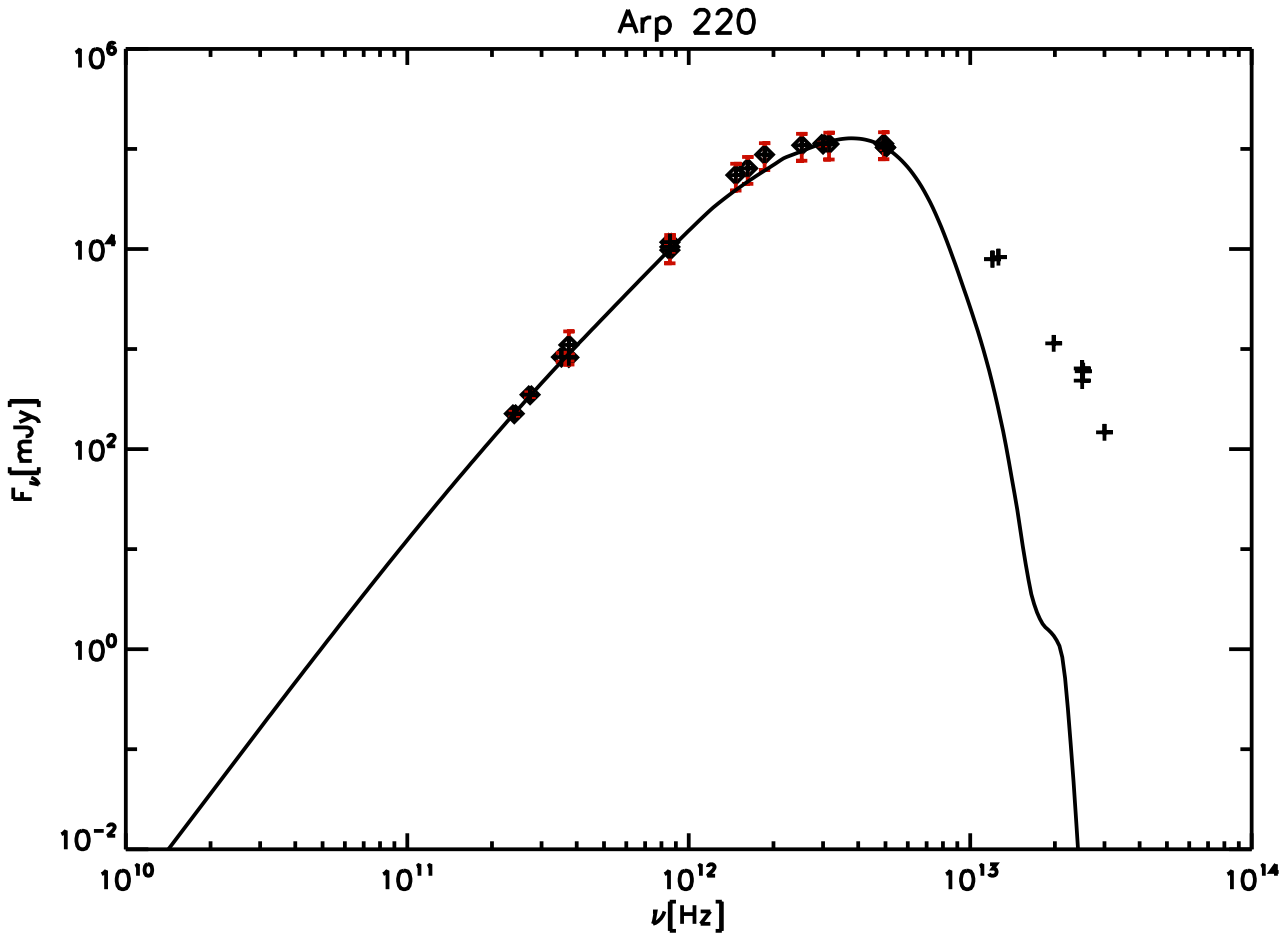

Fig. 3.— Best-fit SED of Arp 220

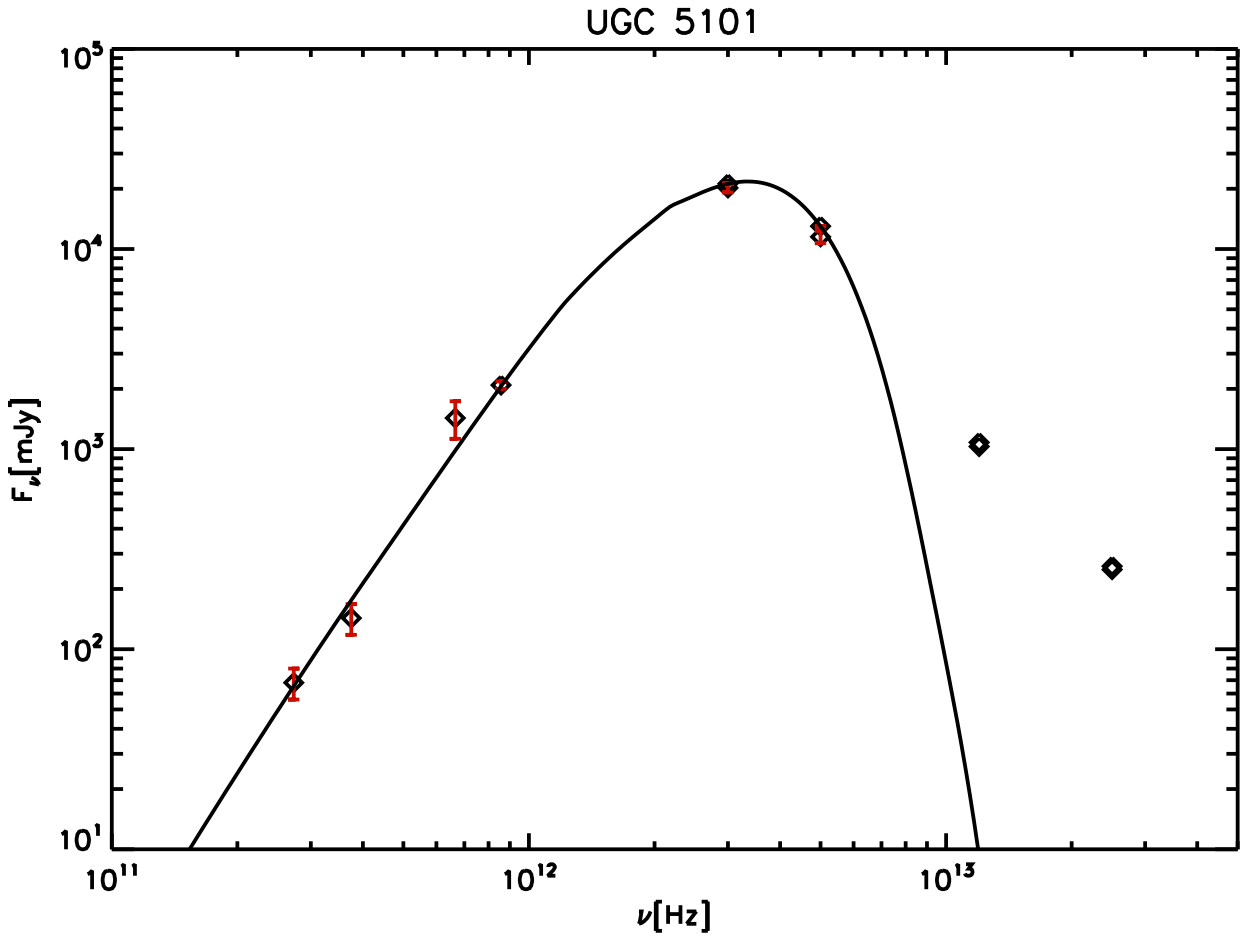

Fig. 4.— Best-fit SED of UGC 5101

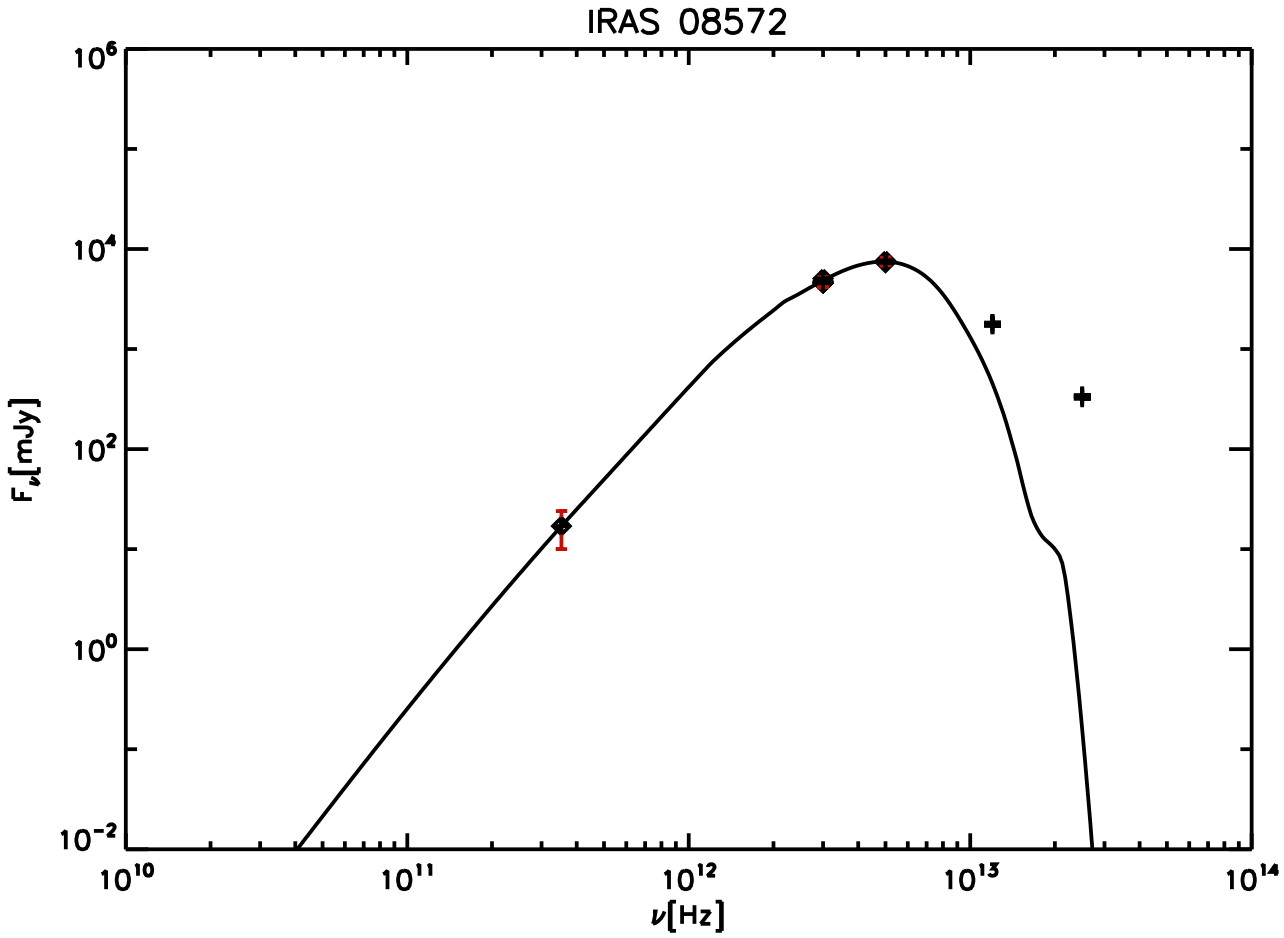

Fig. 5.— Best-fit SED of IRAS 08572+3915

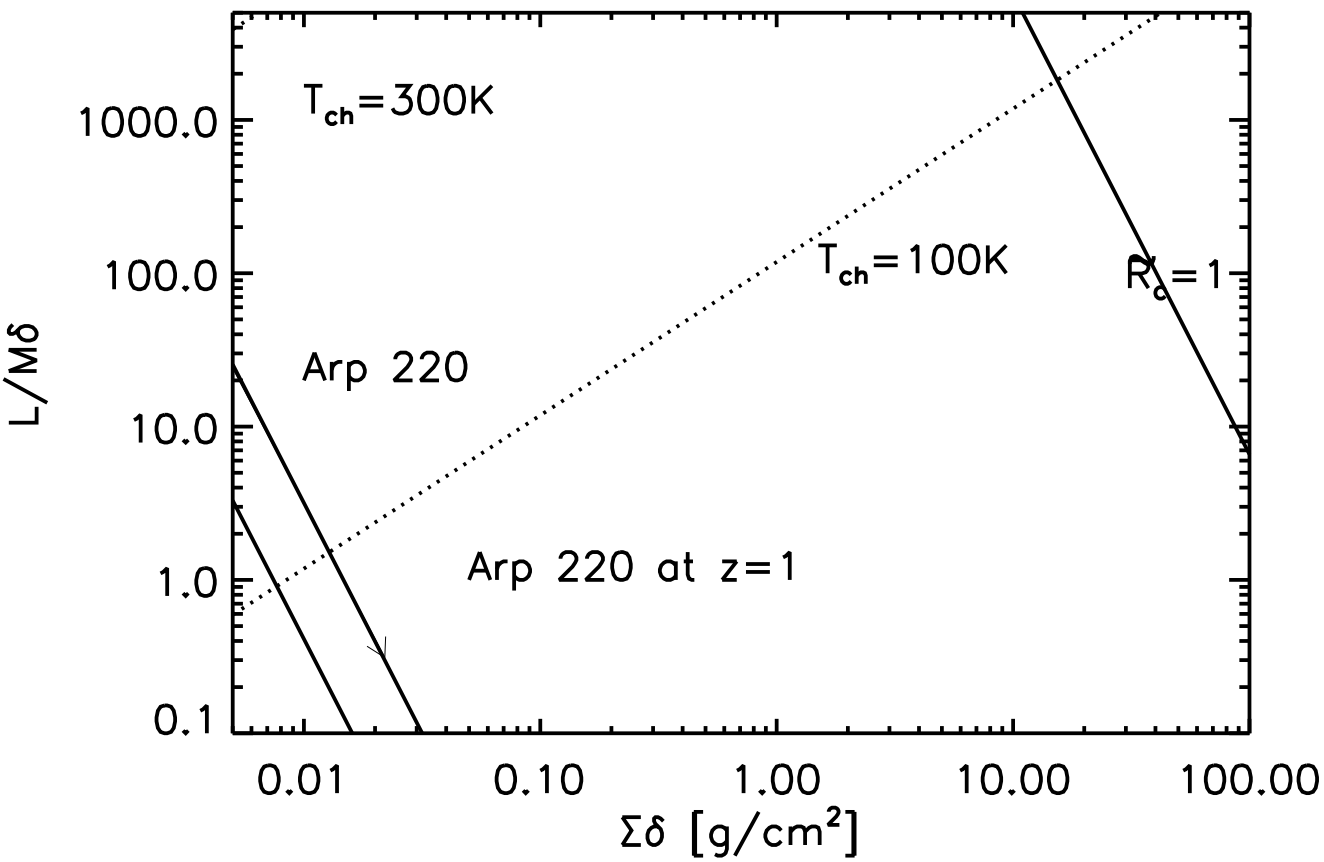

Fig. 6.— Relative change in inferred $L/M\delta$ and $\Sigma\delta$ as Arp 220 is moved from $z = 0.018$ to $z = 1$ (arrow position is at z=1)

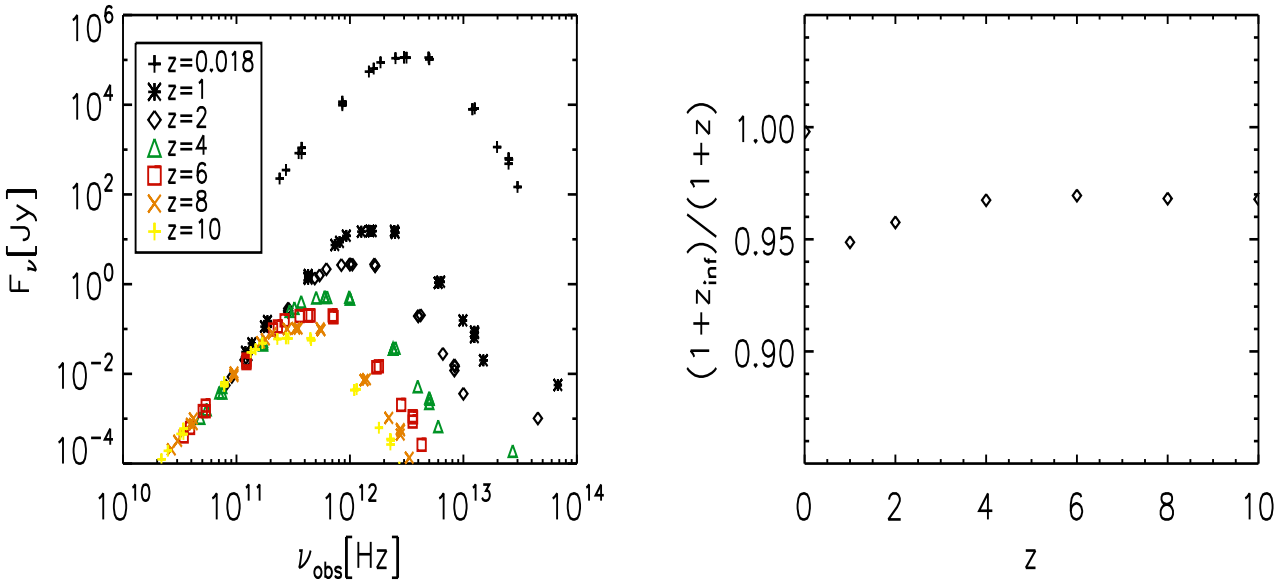

Fig. 7.— (a) SED of Arp220 shifted from $z = 0.018$ to $z = 10$ (b) Resultant inferred redshift compared to the actual redshift.

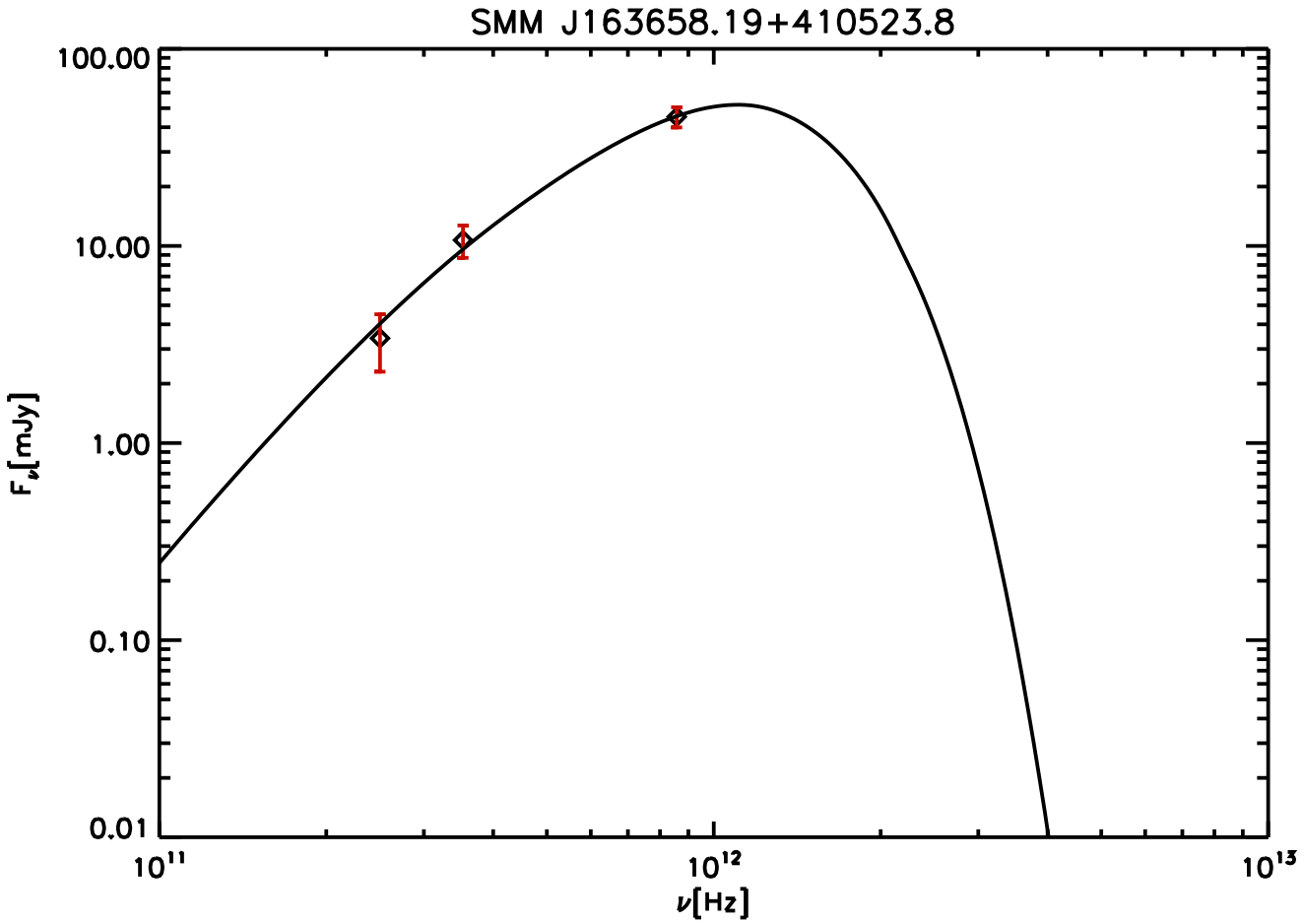

Fig. 8.— Best-fit SED of SMM J163658.19+410523.8

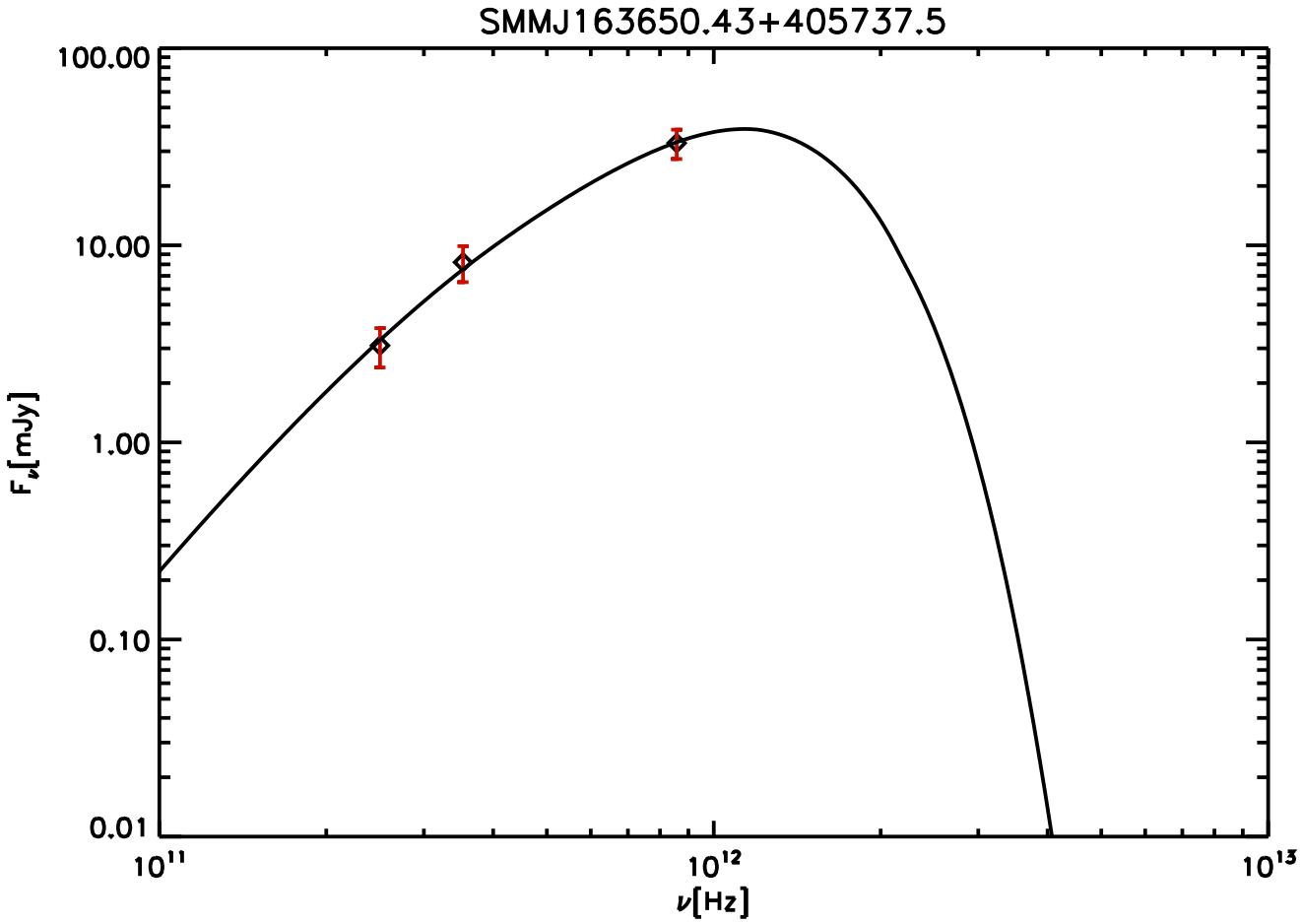

Fig. 9.— Best-fit SED of SMMJ163650.43+405737.5

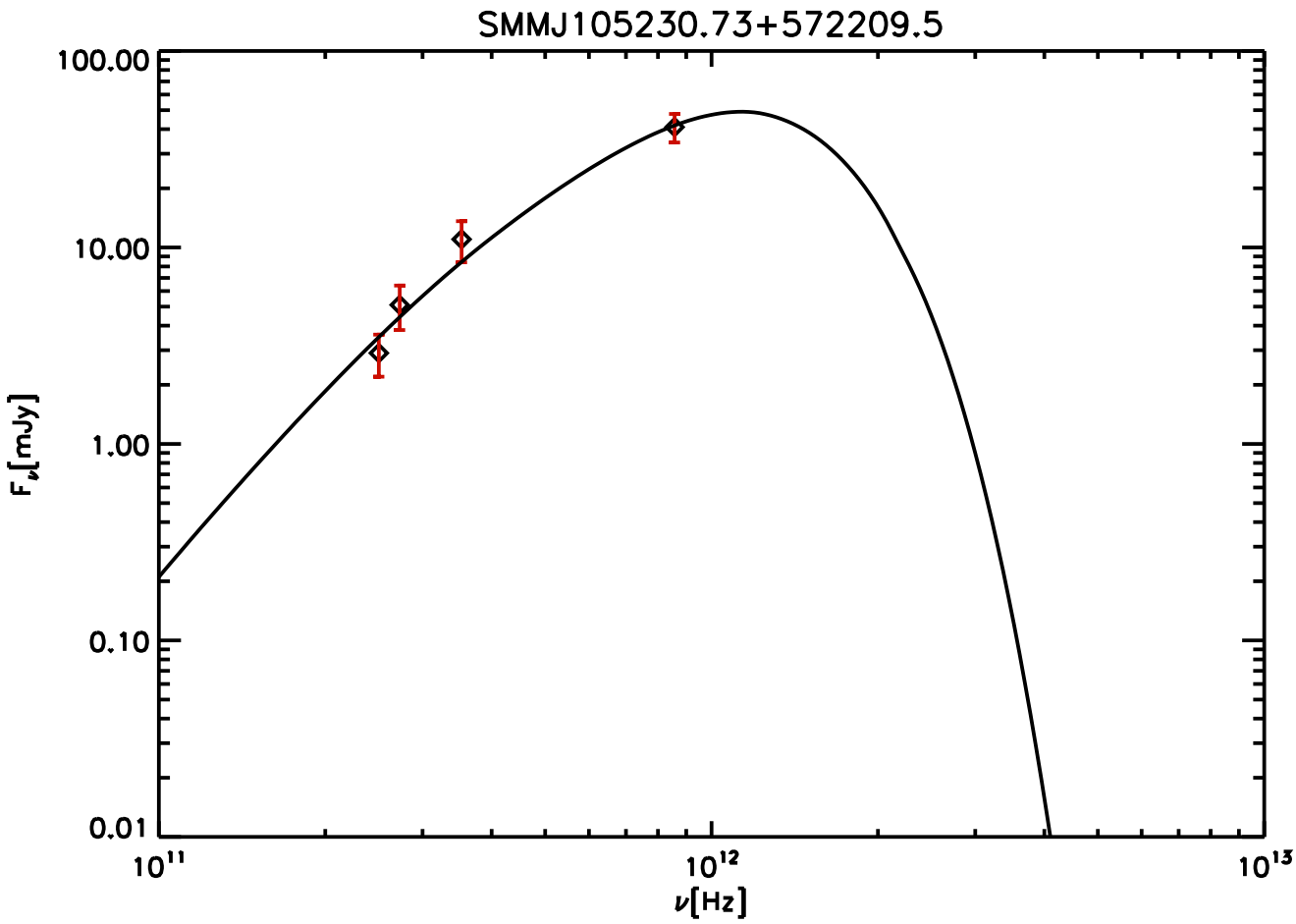

Fig. 10.— Best-fit SED of SMMJ105230.73+572209.5

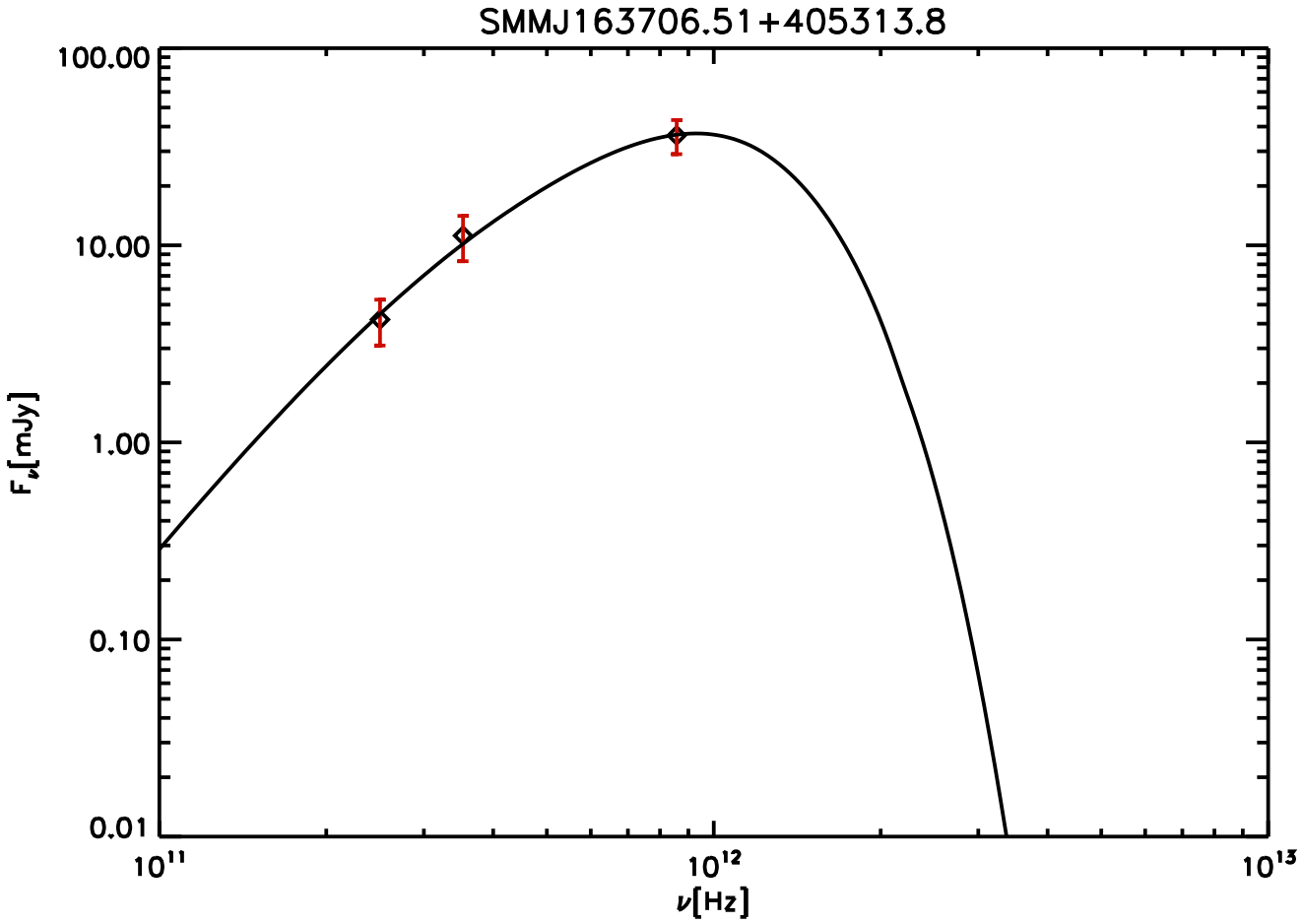

Fig. 11.— Best-fit SED of SMM J163706.51+405313.8

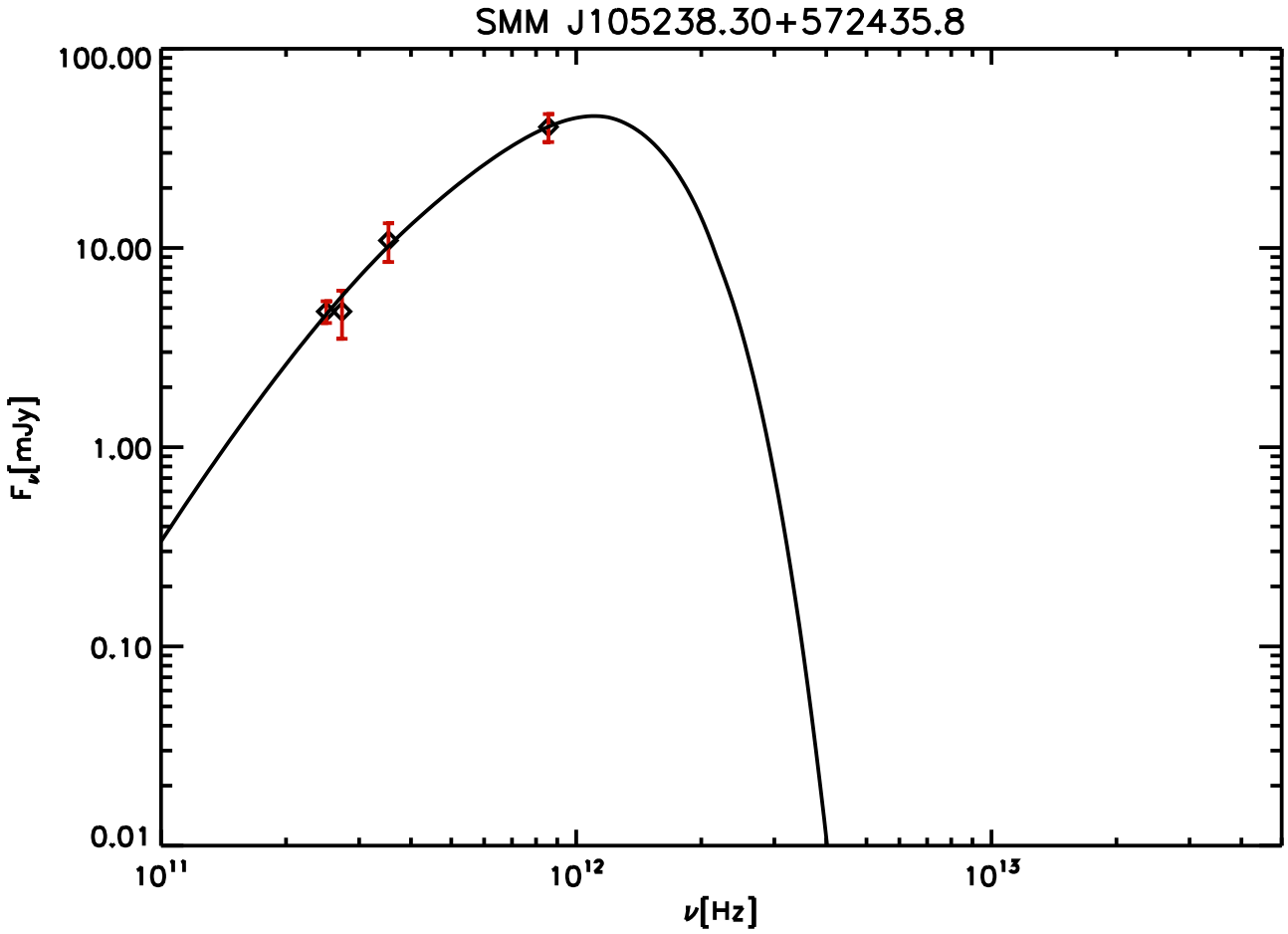

Fig. 12.— Best-fit SED of SMM J105238.30+572435.8

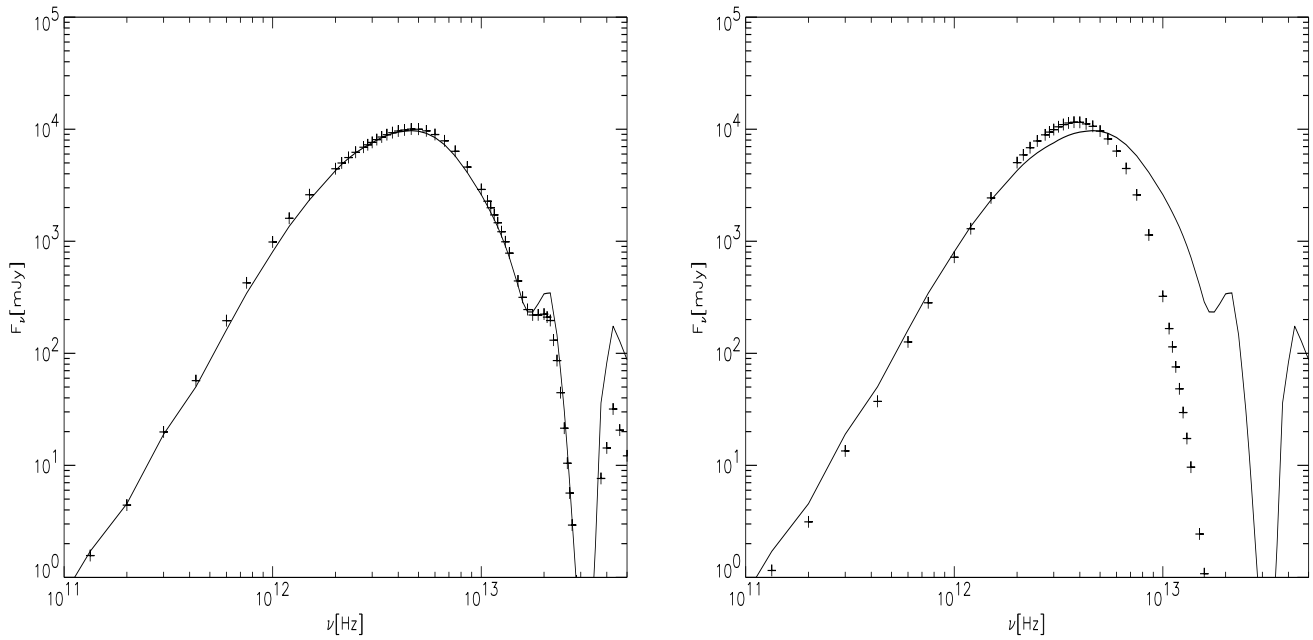

Fig. 13.— (a) SED for large $\tilde{R}_c \sim 300$; solid line is DUSTY, crosses are analytic solution using methodology in CM05. (b) Solid line is DUSTY, crosses are Hildebrand's prescription

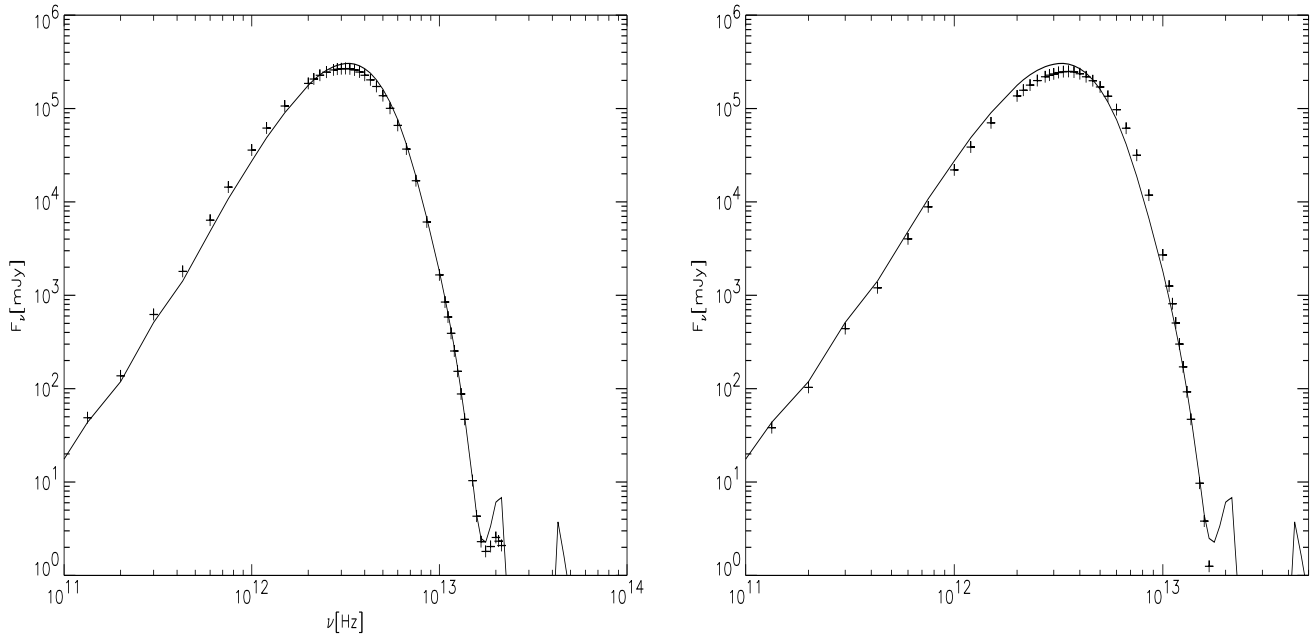

Fig. 14.— (a) SED for low $\tilde{R}_c \sim 10$; solid line is DUSTY, crosses are analytic solution using methodology in CM05. (b) Solid line is DUSTY, crosses are Hildebrand's prescription

REFERENCES

Aaronson, M. & Olszewski, E. W., 1984, Nature, 309, 414A

Armus, L. et al 2004, ApJS, 164, 178A

Babbedge, T.S.R., et al., 2004, MNRAS, 353, 654B

Blain, A.W., et al. 1999, MNRAS, 302, 632 B

Blain, A.W., et al., 2002, PhR, 369, 111B

Bolzonella, M., et al., 2000, A&A, 363, 476B

Bouche, N., et al., 2007, astro-ph/0706.2656

Brodwin, M., et al., 2006, ApJ, 651, 791B

Chakrabarti, S., & McKee, C.F., 2005, ApJ, 631, 792 (CM05)

Chakrabarti, S., Cox, T.J. et. al., 2007a, ApJ, 658, 840C

Chakrabarti, S., Fenner, Y., et al., 2007b, submitted to ApJ, in press, astro-ph/0610860

Chapman, S.C., et al., 2003, Nature, 422, 695C

Chapman, S.C., et al, 2005, ApJ, 622, 772C

Dasyra, K., et al., 2006, ApJ, 638, 745D

Downes, D., & Solomon, P.M., 1998, ApJ, 507, 615D (DS98)

Draine, B.T. & Lee, H.M., 1984, ApJ, 285, 89

Dunne, L., & Eales, S., 2001, MNRAS, 327, 697D

Efstathiou,A. & Rowan-Robinson, M., 2003, MNRAS, 343, 322E

Farrah, D., et al., 2005, ApJ, 626, 70F

Graham, J., et al., 1990, ApJ, 354L, 5G

Hildebrand, R.H., 1983, QJRAS, 24, 267H

Imanishi, M., et al., 2003, ApJ, 596L, 167I

Imanishi, M., & Maloney, P.R., 2003, ApJ, 588, 165I

Ivezic, Z. & Elitzur, M., 1997, MNRAS, 287, 799I

Ivison, R., et al., 2000, MNRAS, 315, 209I

Kovacs, A., et al., 2006, ApJ, 650, 592K

Le Floch, E. et al., 2005, ApJ, 632, 169L

Li A. & Draine, B.T., 2001, ApJ, 554, 778

Mihos, C., & Hernquist, L., 1996, ApJ, 464, 641M

Nesvadba, N., et al., 2007, submitted to ApJ, astro-ph/0708.4150

Rieke, G., & Lebofsky, 1986, ApJ, 304, 326R

Rowan-Robinson, M., 2000, MNRAS, 316, 885R

Sawicki, M., 2002, AJ, 124.3050S

Siebenmorgen, R., & Krugel, E., 2007, A&A, 461, 445S

Sanders, D., & Mirabel, I.F., 1996, ARA&A, 34, 749S

Scoville, N., et al., 1991, ApJ, 366L, 5S

Smail, I., et al. 1997, ApJ, 490L, 5S

Sodroski, T.J, et al., 1997, ApJ, 480, 173S

Soifer, B.T., et al. 1984, ApJ, 278L, 71S

Soifer, B.T., et al., 1987, ApJ, 320, 238S

Soifer, B.T., et al., 1999, ApJ, 513, 207S

Soifer, B.T., et al., 2000, AJ, 119, 509S

Toomre, A., & Toomre, J., 1972, ApJ, 178, 623T

Weingartner, J.C. & Draine, B.T., 2001, ApJ, 548, 296W

Xu, C., Hacking, P.B., Fang, F., Shupe, D.L., Lonsdale, C.J., Lu, N.Y., Helou, G., Stacey, G.J., & Ashby, M., L.N., 1998, ApJ, 508, 579

Xu, C., Lonsdale, C.J., Shupe, D.L., O'Linger, J., Masci, F., 2001, ApJ, 562, 179

Yun, M.S. & Carilli, C.L., 2002, ApJ, 568, 88

This preprint was prepared with the AAS LaTeX macros v5.2.

Table 1. Source Parameters of ULIRGs from SED

Source	L ($L_\odot$)	$M\delta$ ($M_\odot$)	R_c (kpc)	$\Sigma\delta$ (g cm^{-2})	$\tilde{R}_c$	$T_{\rm ch}$
Arp 220	9.4×10^{11}	4.1×10^{10}	10.6	0.025	370 ± 20	125 ± 2.7
UGC 5101	7.1×10^{11}	2.7×10^{10}	5.5	0.07	164 ± 24	112 ± 1.6
IRAS 08572+3915	8.9×10^{11}	6.9×10^{9}	6.6	0.01	470 ± 115	172 ± 4
Mrk 231	1.8×10^{12}	9.9×10^{9}	2.6	0.095	73 ± 19	138 ± 4
Mrk 273	9.7×10^{11}	4.1×10^{10}	13	0.016	509 ± 19	132 ± 2.6
Mrk 1014	2.3×10^{12}	1.4×10^{10}	5.1	0.04	161 ± 96	153 ± 4
IRAS 12112+3035	1.5×10^{12}	2.6×10^{10}	6.5	0.04	191 ± 27	131 ± 2.6
IRAS 00262+4251	8.4×10^{11}	2.0×10^{10}	9.8	0.014	500 ± 50	145 ± 9
IRAS 10565+2448	7.3×10^{11}	9.5×10^{9}	2.5	0.1	85 ± 41	122 ± 2
IRAS 17208-0014	1.8×10^{12}	3.1×10^{10}	6.1	0.05	150 ± 75	128 ± 2

Table 2. Source Parameters of SMGs from SED

Source	L ($L_\odot$)	$M\delta$ ($M_\odot$)	R_c (kpc)	$\Sigma\delta$ (g cm^{-2})	$\tilde{R}_c$	$T_{\rm ch}$
SMMJ163658	$6.8 - 8.2 \times 10^{12}$	$1.3 - 2.6 \times 10^{11}$	5.3-16.0	0.3-0.07	40-150	103-115
SMMJ163650	4.7×10^{12}	1.85×10^{11}	9.1	0.15	85 ± 46	102 ± 7
SMMJ105230	$7.2 - 9.3 \times 10^{12}$	$1.1 - 2.3 \times 10^{11}$	5.0-18.8	0.3-0.04	40-200	107-125
SMMJ163706	4.3×10^{12}	1.6×10^{11}	3.8	0.74	25 ± 16	85 ± 5
SMMJ105238	1.0×10^{13}	2.0×10^{11}	13.4	0.074	122 ± 65	121 ± 8

Table 3. Inferred Redshifts for SMGs

Source	$(1+z_{\rm inf})/(1+z)$(ULIRG norm)	$(1+z_{\rm inf})/(1+z)$(SMG norm)	$z_{\rm spec}$
SMMJ163658	1.02-1.1	0.96-1.04	2.454
SMMJ163650	1.15	1.08	2.376
SMMJ105230	0.98-1.06	0.92-1.00	2.611
SMMJ163706	1.14	1.07	2.374
SMMJ105238	1.03	0.96	3.036